Doklady Physics, Vol. 49, No. 7, 2004, pp. 401–404. Translated from Doklady Akademii Nauk, Vol. 397, No. 1, 2004, pp. 41–44.

PHYSICS

Electron-Excitation Energy Transfer in a Heterocyclic Bichromophore Cooled in a Supersonic Jet

Academician N. A. Borisevich, V. A. Povedaĭlo, V. A. Tolkachev, and D. L. Yakovlev

Received February 10, 2004

In condensed media, the properties of bichromophoric molecules have been investigated rather completely. Electron-excitation energy transfer for molecules with the continuous spectra of absorption and fluorescence is described by the induction resonance and exchange resonance mechanisms [1]. However, the approximations underlying this theory are violated for intermolecular distances comparable with van der Waals radii. In [2, 3], a bichromophoric molecule was considered as a unified system with intramolecular nonradiative energy transport. Recently, electron-energy transport was investigated in aromatic bichromophores cooled in supersonic jets [4, 5].

In the present study, fluorescence polarization was used to investigate electron-excitation energy transfer in bichromophoric heterocyclic molecules cooled in a supersonic jet. The chromophores of these molecules are 2,5 diphenyl oxazole (PPO) and 1-(5'-phenyl-1',3'-oxazole-2'-yl)-4-(5'-phenyl-1',3',4'-oxadiazole-2'-yl)-benzene (POPDP). The PPO and POPDP fragments of the bichromophore are an energy donor and acceptor, respectively. The chromophores are directly coupled with each other by a methylene ($–CH_2–$) bridge. The POPDP absorption spectrum strongly overlaps the PPO fluorescence spectrum in both ethanol solutions and high-temperature vapors, which promotes efficient intermolecular energy transfer. These two compounds are active media for solution lasers, and PPO is also applied in vapor lasers.

The spectrometric equipment for measuring the excitation spectra and degree of fluorescence polarization of complex molecules cooled in a supersonic jet was described in [6]. Vapors of the bichromophore under study were heated to a temperature of 530–570 K, and their mixture with helium at a pressure up to 3 atm was injected into a vacuum chamber by means of a pulsed valve with a nozzle diameter of 0.7 mm. Bichromophoric molecules that do not interact with each other were cooled to 7 K. The molecules under study were excited at a distance of 12 mm from the nozzle by the second harmonic of a dye laser. The spectral-line width of the laser was 1 cm^{-1}, and it could be frequency-tuned within the range 28000–34000 cm^{-1}. The dye laser was pumped by the second harmonic of a pulsed YAG laser. In the process of detecting the rotational contours of electron-transition lines, the spectral width of exciting radiation was equal to 0.08 cm^{-1}. A perpendicular scheme with a Wollaston prism was used to measure the fluorescence polarization.

Figure 1 shows the fluorescence excitation spectra of molecules cooled in a supersonic jet for (a) PPO chromophore, (b) PPO–(CH_2)–POPDP bichromophore, and (c) POPDP chromophore in the bichromophore composition. In this figure, the frequencies of purely electron $\nu_{0–0}$ transitions are imposed on each other, and the relative intensities I_{rel} of the strongest lines in the fluorescence excitation spectra are taken as 1. The fluorescence excitation spectrum corresponds to the molecular absorption spectrum. In the case of cooling molecules in the supersonic jet, the fluorescence excitation spectrum provides information on the structure of the electron vibrational levels of the electron excited state. The purely electron transition occurs when molecules undergo transitions from the zero vibrational level of the ground electron state S_0 to the zero vibrational level of the excited electron state S_n.

Investigation of the fluorescence spectral composition has shown that, in the case of the bichromophore excitation within the absorption range of the PPO donor, only the POPDP acceptor fluoresces, and donor self-fluorescence is not observed. Thus, the total intramolecular singlet–singlet transfer of the electron-excitation energy from the bichromophore donor to the acceptor takes place.

We now analyze in detail the fluorescence excitation spectra shown in Fig. 1. The frequency of the purely electron-transition line of the PPO molecule is $\nu_{0–0}$ =

Institute of Molecular and Atomic Physics, National Academy of Sciences of Belarus, pr. F. Skaryny 70, Minsk, 220072 Belarus

e-mail: bna@presidium.bas-net.by; poved@maph.bas-net.by; tolkachevd@maph.bas-net.by; yakovlev@maph.bas-net.by

1028-3358/04/4907-0401$26.00 © 2004 MAIK “Nauka/Interperiodica”

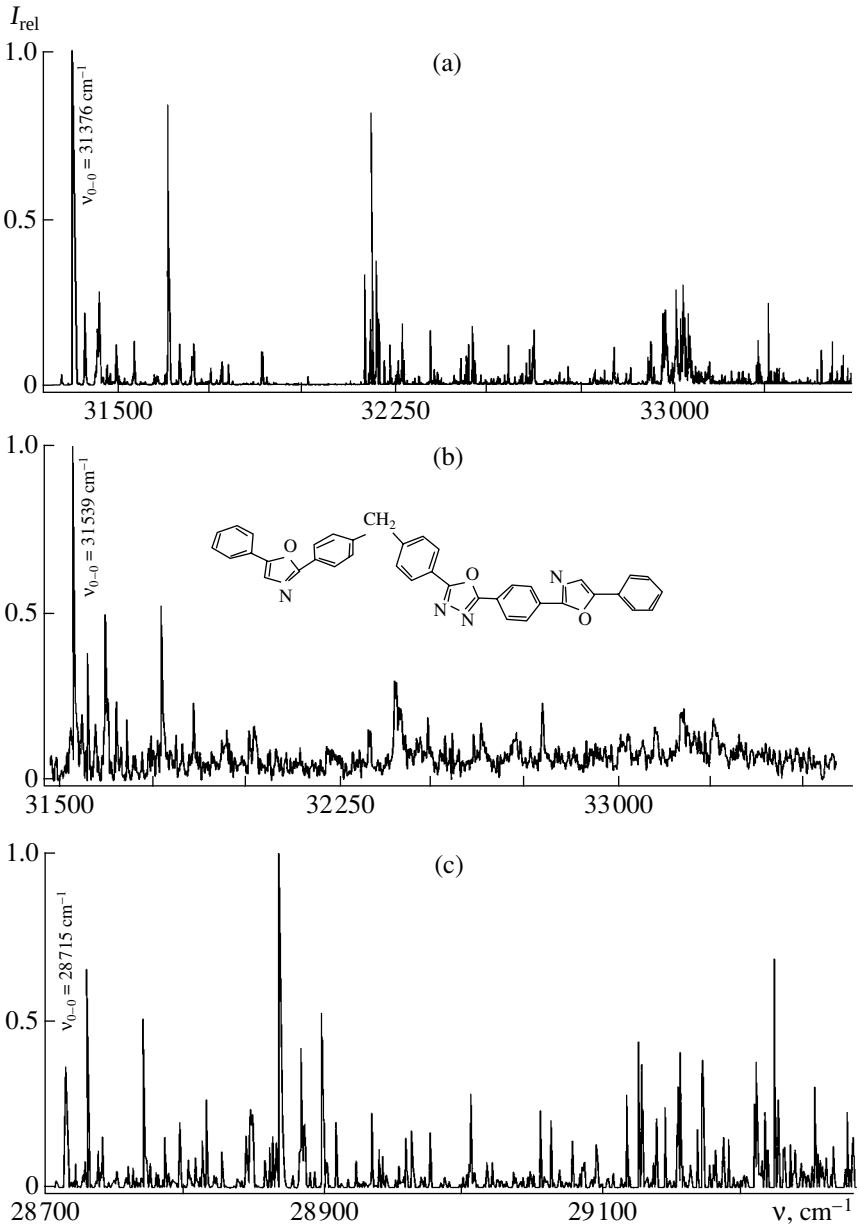

Fig. 1. Fluorescence excitation spectra of heterocyclic molecules cooled in the supersonic jet for (a) PPO, (b) PPO–(CH_2)–POPDP bichromophore, (c) acceptor fragment POPDP of the bichromophore.

31376 cm^{-1}, and for the PPO fragment in the bichromophore, it is 163 cm^{-1} higher and corresponds to 31539 cm^{-1}. In both spectra (see Figs. 1a, 1b), the line of the purely electron transition is the most intense line. For the low-frequency vibration region corresponding to $\nu_{vibr} < 300$ cm^{-1}, there is a group of similar lines in these spectra. The difference between spectra increases with ν_{vibr}, and the vibrational structure virtually disappears in the bichromophore excitation spectrum. The causes of these differences are as follows. In the bichromophore, the POPDP acceptor affects the PPO donor, because they reside in the same molecule. The acceptor fluoresces due to excitation energy transfer from PPO. The spectrum of the direct excitation of the acceptor fluorescence is presented in Fig. 1c. The frequency of the purely electron transition is ν_{0-0} = 28715 cm^{-1} and is 2824 cm^{-1} lower than ν_{0-0} of PPO. When the electron-excitation energy is transferred from the donor, the acceptor acquires a considerable reserve of the vibrational energy and excited molecules are in the high-density region of the vibrational states. In the fluorescence time, which is equal to about 10^{-9} s, the intramolecular redistribution of the vibrational-energy reserve occurs. The redistribution rate increases with the reserve and can be higher than the fluorescence rate by 3–4 orders of magnitude. This results in spreading

of the vibrational structure of the bichromophore fluorescence excitation spectrum. In the case of direct acceptor excitation, the POPDP energy spectrum has a pronounced vibrational structure (Fig. 1c).

When complex molecules are cooled in the supersonic jet down to the temperatures indicated above, the molecules preserve their rotational capability. Contours of their lines corresponding to purely electron transitions can have the rotational structure consisting of *P*, *Q*, and *R* branches. In the bichromophore fluorescence excitation spectrum, the rotational contour of the line corresponding to the purely electron transition of the donor fragment (PPO) exhibits no rotational structure and is significantly broader than the rotational contour of the acceptor (POPDP) fragment line. In the former case, the measured value of the contour half-width is 2.8 cm^{-1}, whereas in the latter case, it does not exceed 0.7 cm^{-1}. The line broadening is caused by the short lifetime $\Delta t \approx 2 \times 10^{-12}$ s of the excited electron state, which is calculated on the basis of the uncertainty principle $\Delta E \cdot \Delta t \geq \frac{\hbar}{2\pi}$. Therefore, electron-excitation energy is transferred from the donor to the acceptor in a time three orders of magnitude shorter than the lifetime of the S_1 state of high-temperature PPO vapors [7].

Curve *1* in Fig. 2 shows the measured rotational contour of the ν_{0-0} line corresponding to the purely electron transition in the fluorescence excitation spectrum of jet-cooled PPO molecules. The temperature of saturated PPO vapors was equal to 373 K, and the pressure of the helium gas carrier was equal to 3 atm. Under these experimental conditions, the *P*, *Q*, and *R* branches of the ν_{0-0} line are clearly manifested and the contour half-width corresponds to 0.5 cm^{-1}. Curve *2* presents the calculated *P* and *R* branches. The calculation is performed in the approximation of a rigid asymmetric molecular top. For this model, the *Q* branch is represented by a line [8]. Due to the flexibility of actual molecules, their *Q* branch is always broadened. The measured and calculated intensities I_{rel} of the *P* and *R* branches, as well as distances between them, correlate at a rotational temperature of 2 K.

The calculated dependence of the degree of fluorescence polarization P_f on the frequency of linearly polarized exciting radiation within the rotational contour of the line for the purely electron S_0–S_1 transition of jet-cooled PPO molecules is presented by curve *3* in Fig. 2. The open circles in Fig. 2 correspond to the experimental values of P_f. In the *Q* branch, the calculated value $P_f = 6.1\%$ is marked by an asterisk. The close value $P_f = 5.9\%$ is obtained experimentally in the *Q*-branch maximum. For the *P* and *R* branches, polarizations are higher and are, on average, equal to about 8.5%. They decrease with approaching the *Q* branch. The satisfactory consistency of the experimental and calculated values of P_f within the rotational contour of the line corresponding to the purely electron transition corroborates that oscillators responsible for absorptive S_0–S_1 and emissive S_1–S_0 electron transitions are parallel to each other and directed along the axis of the minimum principal moment of inertia of the PPO molecule. The arrangement of oscillators in the POPDP molecule is similar.

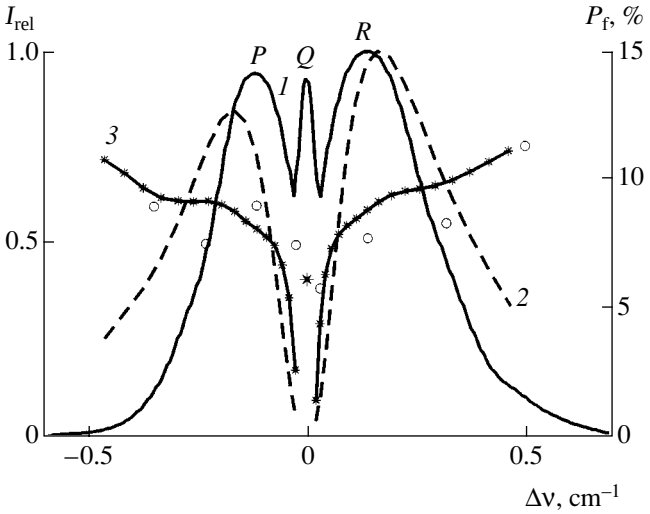

Fig. 2. (*1*) Measured and (*2*) calculated rotational contour for the line of the purely electron transition and the (open circles) measured and (*3*) calculated fluorescence polarization degree for PPO molecules cooled in the supersonic jet; *P, Q,* and *R* are branches of the rotational contour for the line of the purely electron transition.

Linearly polarized radiation with a spectral width of 0.08 cm^{-1} excites the PPO donor of the bichromophore at the frequency of the purely electron transition, and the measured degree of fluorescence polarization is equal to $P_f \approx 5\%$ within the entire rotational contour. The same value of P_f is found in the case of excitation of the PPO donor by broadband radiation. This result testifies to both broadening the rotational contour of the ν_{0-0} line due to the short lifetime of the excited state of the donor fragment of the bichromophore and overlapping *P, Q,* and *R* branches. For the direct excitation of the POPDP acceptor fragment of the bichromophore at the frequency ν_{0-0} by broadband radiation, the measured degree of fluorescence polarization is equal to 8.2%.

Thus, in the case of direct excitation, the degree of fluorescence polarization of both PPO molecules and the POPDP fragment of the bichromophore is higher than that of the PPO–(CH_2)–POPDP bichromophore. This result additionally confirms the intramolecular singlet–singlet excitation-energy transfer in bichromophoric heterocyclic molecules cooled in the supersonic jet.

ACKNOWLEDGMENTS

This work was supported by the International Science and Technology Center, project no. V-441.

REFERENCES

1. V. L. Ermolaev, E. N. Bodunov, E. B. Svershnikova, and T. A. Shakhverdov, *Nonradiative Transfer of the Electron Excitation Energy* (Nauka, Leningrad, 1977).
2. S. Speiser, Chem. Rev. **96**, 1953 (1996).
3. G. V. Maĭer, V. Ya. Artyukhov, O. K. Bazyl', *et al.*, *Electron Excited States and Photochemistry of Organic Compounds* (Nauka, Novosibirsk, 1997).
4. N. A. van Dantzig, D. H. Levy, C. Vigo, and P. Piotrowiak, J. Chem. Phys. **103**, 4894 (1995).
5. S. S. Panja and T. Chakraborty, J. Chem. Phys. **118**, 6200 (2003).
6. N. A. Borisevich, S. L. Derzhitskiĭ, V. A. Povedaĭlo, and V. A. Tolkachev, Zh. Prikl. Spektrosk. **69**, 493 (2002).
7. V. V. Gruzinskiĭ and L. A. Barkova, Zh. Prikl. Spektrosk. **19**, 254 (1973).
8. V. A. Tolkachev, Zh. Prikl. Spektrosk. **70**, 469 (2003).

Translated by G. Merzon

Doklady Physics, Vol. 49, No. 7, 2004, pp. 405–408. Translated from Doklady Akademii Nauk, Vol. 397, No. 2, 2004, pp. 186–190.

PHYSICS

External Feedback Effect on Magnetic Islands in Tokamaks

S. V. Konovalov[1,2], A. B. Mikhaĭlovskiĭ[2,3,*], E. A. Kovalishen[2,3], F. F. Kamenets[3], T. Ozeki[1], M. S. Shirokov[2,4], T. Takizuka[1], and V. S. Tsypin[5]

Presented by Academician A.M. Fridman January 12, 2004

Received February 16, 2004

1. INTRODUCTION

As is known (see, e.g., [1] and references cited therein), magnetic islands limit attainable plasma pressure in tokamaks. Therefore, their suppression is one of the main problems of recent studies of the tokamak plasma. The most advanced method of such a suppression is based on using the effect of the electron cyclotron current drive (see, e.g., [1] and references cited therein). At the same time, according to theoretical works [2, 3] and a series of similar investigations appealing to experimental work [4] on the feedback suppression of kink instability, magnetic islands including neoclassical tearing modes (NTMs) are sensitive to external magnetic fields whose helicity coincides with the helicity of the island fields. Similarly to [4], these papers suggested a feedback system with control coils placed inside the vacuum vessel (internal feedback system). However, the internal disposal of the control coils is hardly possible under reactor conditions [5]. Then, it is reasonable to consider an alternative external arrangement of the control coils (external feedback) similar to that successfully used for the stabilization of resistive wall modes (RWMs) in the DIII-D tokamak [6].

Theoretical study of the external feedback effect on NTMs in tokamaks is the goal of this paper. To some extent, our problem is similar to the feedback suppression of external RWMs considered in [7, 8] and some other papers. In contrast to NTMs, in the case of external RWMs, the singular point of the mode lies outside the wall.

The main essence of our analysis is to derive the so-called external matching parameters of the island chain [1] in the presence of the external feedback system and introduce them into the evolution equations for the island width and island rotation frequency. In addition, the complex external matching parameter derived in this work can be used in analysis of linear resistive wall drift-tearing modes (internal RWMs) discussed in [9].

Discussion of a particular control algorithm of the feedback system is beyond the scope of this paper. We focus on stationary states of NTMs, which can be reached in the presence of the control coil current of a given amplitude. In this context, we use the term "feedback," assuming that the magnetic field produced by the control coils is always in phase with the rotating mode.

[1] *Naka Fusion Research Establishment, Japan Atomic Energy Research Institute, Ibaraki 3111-0193, Japan*

[2] *Institute of Nuclear Fusion, Russian Research Centre Kurchatov Institute, pl. Kurchatova 1, Moscow, 123182 Russia*

[3] *Nonlinear Physics Laboratory, Moscow Institute of Physics and Technology, Institutskiĭ per. 9, Dolgoprudnyĭ, Moscow oblast, 141700 Russia*

[4] *Department of Plasma Physics, Moscow Engineering Physics Institute, Kashirskoe sh. 31, Moscow, 115409 Russia*

[5] *Physics Institute, University of São Paulo, Cidade Universitaria, 05508-900, São Paulo, Brazil*

* *e-mail: mikh@nfi.kiae.ru*

2. EXTERNAL MATCHING PARAMETERS IN THE PRESENCE OF THE FEEDBACK SYSTEM

2.1. Description of the Perturbed Magnetic Field Far from the Island Chain

For simplicity, the external matching parameters are derived in the cylindrical approximation. In this case, the equilibrium magnetic surfaces are characterized by the radial coordinate r. One more simplification concerns the profile of the equilibrium parallel current density $j_\parallel(r)$. Similarly to [7], we consider the step profile $j_\parallel(r)$ defined by the conditions $j_\parallel = \text{const}$ for $0 < r < r_0$ and $j_\parallel = 0$ for $r > r_0$, where r_0 is the current channel radius. In this case, the safety factor profile $q(r)$ is given

1028-3358/04/4907-0405$26.00 © 2004 MAIK "Nauka/Interperiodica"

as $q(r) = q_0$ for $r < r_0$ and $q = q_0\left(\frac{r}{r_0}\right)^2$ for $r > r_0$, where $q_0 \equiv q(r_0)$ is a constant.

It is assumed that a rational magnetic surface, $r = r_s$, where $q(r_s) =$ and m and n are integers ($m > 0$), exists between the surface $r = r_0$ and the plasma boundary $r = a$. This surface centers the chain of magnetic islands characterized by the island magnetic flux function $\psi = \hat{\psi}(r_s) - \frac{x^2 B_0}{2L_s}$. Here, $\hat{\psi}(r_s) = \tilde{\psi}\cos\xi$, where $\tilde{\psi}$ is the positive constant characterizing the perturbation amplitude and $\xi \equiv m\theta - n\zeta - \omega t$ is the island cyclic variable, where θ and ζ are the poloidal and toroidal angles, respectively, and ω is the island rotation frequency; $x = r - r_s$; B_0 is the equilibrium magnetic field; and L_s is the magnetic shear length.

Following Section 27.1.1 of [10], we find that the perturbed magnetic flux function $\hat{\psi}(r)$ is given by $\hat{\psi} = \psi^-(r)$

$$\psi^-(r) = \tilde{\psi}\left(\frac{r}{r_s}\right)^m \frac{m - nq_0 - 1 + \left(\frac{r_0}{r}\right)^{2m}}{m - nq_0 - 1 + \left(\frac{r_0}{r_s}\right)^{2m}} \quad (1)$$

for $r_0 < r < r_s$ and $\hat{\psi} = \psi^+(r)$

$$\psi^+(r) = \frac{\tilde{\psi}}{(1-z)(\hat{\omega} + i)} \times \left\{\left(\frac{r_s}{r}\right)^m [\hat{\omega} + i(1-z) + iz^{1/2}(1-z)\hat{j}_{fb}] - \left(\frac{r}{r_s}\right)^m z^{1/2}[z^{1/2}\hat{\omega} + i(1-z)\hat{j}_{fb}]\right\} \quad (2)$$

for $r_s < r < a$. Here, $z = \left(\frac{r_s}{a}\right)^{2m}$, $\hat{\omega} = \frac{(1-z)\omega}{2m\gamma_d}$, $\gamma_d = \frac{c^2}{4\pi\sigma_w a d}$ is the wall diffusion decay rate, c is the speed of light, d is the wall thickness, and σ_w is the wall electric conductivity. The parameter $\hat{j}_{fb}$ determines the relative power of the feedback system and is defined by

$$\hat{j}_{fb} = \frac{2\pi a J_{fb}}{mc\tilde{\psi}}; \quad (3)$$

where J_{fb} is the surface feedback current related to the volume current density j_{fb} as

$$J_{fb} = \int_{a+d}^{a_*} j_{fb} dr. \quad (4)$$

Here, $a_* = a + d + \delta$, where δ is the radial width of the control coil arrangement, which is assumed to be much smaller than the plasma radius, $\delta \ll a$. Similarly to [7], we assume that the feedback control coils are placed immediately behind the wall (the case with control coils located at a certain distance from the wall was considered in [8]). We consider that the feedback sensors measure the radial magnetic field component B_r.

2.2. Complex External Matching Parameter in the Presence of the Feedback System

Introducing the complex external matching parameter as

$$\hat{\Delta}' = \frac{1}{\tilde{\psi}}\left(\frac{d\psi^+}{dr} - \frac{d\psi^-}{dr}\right)\Bigg|_{r = r_s}, \quad (5)$$

and using Eqs. (1) and (2), we obtain

$$\hat{\Delta}' = \hat{\Delta}'_0 + \hat{\Delta}'_{fb}. \quad (6)$$

Here,

$$\hat{\Delta}'_0 = \Delta'_w + i\frac{\Delta'_\infty - \Delta'_w}{\hat{\omega} + i} \quad (7)$$

is the standard expression for Δ' calculated in the absence of the feedback system [11] and

$$\hat{\Delta}'_{fb} = -\frac{2imz^{1/2}\hat{j}_{fb}}{r_s(\hat{\omega} + i)} \quad (8)$$

describes the contribution of the feedback system. In Eq. (7),

$$\Delta'_w = -2\frac{m}{r_s}\frac{m - nq_0 - 1 + \left(\frac{r_0}{a}\right)^{2m}}{(1-z)\left[m - nq_0 - 1 + \left(\frac{r_0}{r_s}\right)^{2m}\right]}, \quad (9)$$

$$\Delta'_\infty = -2\frac{m}{r_s}\frac{m - nq_0 - 1}{m - nq_0 - 1 + \left(\frac{r_0}{r_s}\right)^{2m}} \quad (10)$$

are the external matching parameters for the ideally conductive wall and absence of the wall, respectively [11]. Expressions (9) and (10) are relevant only to the step profile $j_\parallel(r)$, while Eq. (7), relating $\hat{\Delta}'_0$ with $\hat{\Delta}'_\infty$ and Δ'_w, is valid for arbitrary current profile. Additional analysis shows that Eq. (8) is valid for the internal feedback system.

In accordance with the above discussion, Eq. (6) can be used in both the linear problem of internal RWMs and nonlinear problems. Below, we use it in the nonlinear problem of the NTM stationary state.

3. NTM STATIONARY STATE IN THE PRESENCE OF THE FEEDBACK SYSTEM

3.1. Island Dynamic Equations in Terms of Matching Parameters

The dynamics of magnetic islands is determined by the island width evolution equation and island rotation frequency equation. According to [1], they can be represented in the form

$$\Delta_c^{int} = \mathrm{Re}\hat{\Delta}', \quad (11)$$

$$\Delta_s^{int} = \mathrm{Im}\hat{\Delta}', \quad (12)$$

respectively. Here, Δ_c^{int} and Δ_s^{int} are the cos and sin parts of the internal matching parameter of the island chain, respectively. In order to introduce the feedback effect into these equations, one should separate expression (8) into the real and imaginary parts

$$\mathrm{Re}\hat{\Delta}'_{fb} = \frac{2k_y z^{1/2}}{\hat{\omega}^2 + 1}(\hat{\omega}\hat{j}_{fbI} - \hat{j}_{fbR}), \quad (13)$$

$$\mathrm{Im}\hat{\Delta}'_{fb} = -\frac{2k_y z^{1/2}}{\hat{\omega}^2 + 1}(\hat{\omega}\hat{j}_{fbI} + \hat{j}_{fbI}), \quad (14)$$

where $\hat{j}_{fbR}$ and $\hat{j}_{fbI}$ are the real and imaginary parts of $\hat{j}_{fb}$, respectively, and $k_y \equiv \frac{m}{r_s}$. Similar separation of the complex quantity $\hat{\Delta}'_0$ given by Eq. (7) yields

$$\mathrm{Re}\hat{\Delta}'_0 = \Delta'_\infty - \frac{\hat{\omega}^2}{1 + \hat{\omega}^2}(\Delta'_\infty - \Delta'_w), \quad (15)$$

$$\mathrm{Im}\hat{\Delta}'_0 = \frac{\hat{\omega}}{1 + \hat{\omega}^2}(\Delta'_\infty - \Delta'_w). \quad (16)$$

As is seen from Eqs. (13)–(16), our problem depends essentially on the parameter $\hat{\omega}$, which physically means the ratio of the mode frequency to the wall diffusion decay rate. According to the estimates made in [9] under the assumption that the mode frequency is of the order of the characteristic diamagnetic drift frequency ω_*, $\omega \simeq \omega_*$, this parameter is about unity for current experimental devices (ASDEX-U, DIII-D, JET, TFTR, JT-60U). In this case, the feedback effect should be considered at $\hat{\omega} \simeq 1$. At the same time, it follows from [9] that the approximation $\hat{\omega} \gg 1$ is typical for reactor applications. According to [9], the toroidal plasma rotation effect can significantly modify the above estimates.

It is seen from Eqs. (13) and (14) that the feedback effect disappears for $\hat{\omega} \longrightarrow \infty$. Nevertheless, the value $\mathrm{Im}\hat{\Delta}'_{fb}$ can be important in this case, because the quantity Δ_s^{int} [see Eq. (12)], describing the dissipative plasma response, is relatively small for a high performance plasma [1]. Considering Eqs. (14) and (15), one can find that

$$\mathrm{Im}\hat{\Delta}'_{fb} = -\frac{2k_y z^{1/2}\hat{j}_{fbR}}{\hat{\omega}}, \quad (17)$$

$$\mathrm{Im}\hat{\Delta}'_0 = \frac{2k_y z}{(1-z)\hat{\omega}} \quad (18)$$

for $\hat{\omega} \gg 1$. According to Eqs. (17) and (18), when the external feedback effect can be important, $\hat{j}_{fb} \gtrsim 1$. Considering Eq. (3) and taking into account that $\tilde{\psi} = \frac{W^2 B_0}{16 L_s}$ (W is the island width) [1], one can see that the minimum current in the feedback control coils J_{fb}^{min} is proportional to the squared island width, $J_{bs}^{min} \sim W^2$. Nevertheless, the feedback system cannot be applied in the case of very narrow islands because of the sensibility threshold of sensors measuring the field $B_r(a)$: $B_r(a)$ vanishes in the limit $W \longrightarrow 0$ for $\hat{j}_{fb} \simeq 1$.

3.2. Banana Regime

Under the assumption that the rotation frequency is sustained as a result of competition between dissipative effects related to parallel plasma viscosity and the wall resistivity, an example of the stationary island rotation frequency equation following from Eq. (12) in the absence of the feedback system was analyzed recently in [12]. In the presence of the feedback effect, this equation is generalized as

$$c_\parallel \frac{[\omega - \omega_{*i}(1 + k_1\eta_i) + n\Omega_T]\chi_\theta^b}{k_y^3 w^3 \omega_A^2} + \frac{1}{\hat{\omega}}\left\{1 - \left(\frac{a}{r_s}\right)^m\left[1 - \left(\frac{r_s}{a}\right)^{2m}\right]\hat{j}_{fbR}\right\} = 0. \quad (19)$$

Here, it is assumed that the plasma rotates in the toroidal direction with the angular frequency Ω_T; $w = \frac{W}{2}$ is the island half-width; ω_A is the Alfvén frequency; $c_\parallel = 6.14$ [12]; ω_{*i} is the ion diamagnetic drift frequency determined by the density gradient; η_i is the relative ion temperature gradient; k_1 is a numerical coefficient, which, in accordance with [3, 12], is equal to $k_1 = 1.17$; and $\chi_\theta^b \simeq \frac{q^2 \nu_i}{\varepsilon^{3/2}}$ is the poloidal viscosity coefficient, where ν_i is the ion collision frequency and ε is the inverse aspect ratio for $r = r_s$.

The feedback effect is introduced into the island width equation for arbitrary $\hat{\omega}$ through Eq. (11). For

$\hat{\omega} \gg 1$, such an introduction is insignificant, so that, for the case of stationary island width, this equation reduces to [1]

$$\frac{\Delta'}{4} + \Delta_{bs} + \Delta_p = 0. \quad (20)$$

The quantities Δ_{bs} and Δ_p are the bootstrap current and polarization current contributions, respectively. Up to positive multipliers independent of the island rotation frequency, they are given by

$$\Delta_{bs} \sim \frac{w}{w^2 + w_c^2(\omega)} + \Delta_{bs}^{visc}(\omega), \quad (21)$$

$$\Delta_p \sim \frac{1}{w^3}(\omega + n\Omega_T)[\omega + n\Omega_T - \omega_{*i}(1 + k_2\eta_i)]. \quad (22)$$

Here, $w_c(\omega)$ is the critical island half-width related to the finite perpendicular heat transport which, according to [1, 13, 14], is sensitive to effects dependent on island rotation frequency; Δ_{bs}^{visc} is the viscosity-dependent part of the bootstrap drive of the mode [15]; and k_2 is a collisionality-dependent numerical coefficient [1]. A more detailed structure of the value Δ_p can be found by using [1, 3].

4. DISCUSSION

Equation (19) shows that the feedback effect can lead to the shift of the rotation frequency of NTMs. Thereby, the feedback system can be used to control the polarization current effect [1, 3], which, according to Eq. (22), is stabilizing or destabilizing, depending on the sign and value of the island rotation frequency. Thus, it is of interest to study the more general problem of the feedback modification of the polarization current threshold model of NTMs [1].

According to Eq. (21), the island rotation frequency is also essential for theories appealing to the transport threshold model of NTMs [1, 13, 14]. Therefore, further development of these theories with allowance for the feedback effect on the island rotation frequency seems to be important.

We have limited our analysis of the magnetic island problem by assuming $\hat{\omega} \gg 1$ and neglecting the feedback term in Eq. (11) for the island width. Meanwhile, varying the island rotation frequency, it is possible to achieve the regime $\hat{\omega} \simeq 1$ and thereby to introduce the feedback contribution into the island width equation. Analysis of such a possibility can be one more topic of further investigations of the external feedback effect.

ACKNOWLEDGMENTS

We are grateful to R.M.O. Galvão and I.C. Nascimento for stimulating discussions. A.B.M. thanks the Japan Atomic Energy Research Institute for hospitality and support under the JAERI Foreign Researcher Inviting Program while performing this work.

This work was supported by the Russian Foundation for Basic Research (project no. 03-02-16294), the Council of the President of the Russian Federation for Support of Young Russian Scientists and Leading Scientific Schools (project no. NSh-2024.2003.2), the Department of Atomic Science and Technology of the Russian Ministry of Atomic Industry, the US Civilian Research and Development Foundation for the Independent States of the Former Soviet Union (grant no. BRHE REC-011), the Excellence Research Program (PRONEX) of the Brazilian National Council of Scientific and Technological Development (CNPq), and the São Paulo State Research Foundation (FAPESP), Brazil.

REFERENCES

1. A. B. Mikhailovskii, Contrib. Plasma Phys. **43**, 125 (2003).
2. E. Lazzaro and M. F. F. Nave, Phys. Fluids **31**, 1623 (1988).
3. A. I. Smolyakov, A. Hirose, E. Lazzaro, *et al.*, Phys. Plasmas **2**, 1581 (1995).
4. V. V. Arsenin, L. I. Artemenkov, N. V. Ivanov, *et al.*, in *Proceedings of the 7th International Atomic Energy Agency (IAEA) Conference on Plasma Physics and Controlled Nuclear Fusion, Innsbruck, 1978* (IAEA, Vienna, 1979), Vol. 1, p. 233.
5. *ITER Technical Basis, Plant Description Document*, Chap. 3.7.4.1.4, in *ITER EDA Documentation Ser.* (IAEA, Vienna, 2002), No. 24.
6. E. J. Strait, J. Bialek, N. Bogatu, *et al.*, Nucl. Fusion **43**, 430 (2003).
7. A. B. Mikhaĭlovskiĭ and B. N. Kuvshinov, Plasma Phys. Rep. **22**, 172 (1996).
8. A. B. Mikhaĭlovskiĭ and V. D. Pustovitov, Plasma Phys. Rep. **26**, 477 (2000).
9. S. V. Konovalov, A. B. Mikhaĭlovskiĭ, V. S. Tsypin, *et al.*, Plasma Phys. Rep. **29**, 779 (2003).
10. A. B. Mikhailovskii, *Instabilities in a Confined Plasma* (Inst. Phys., Bristol, 1998).
11. P. H. Rutherford, in *Proceedings of the Course and Workshop on Basic Physical Processes of Toroidal Fusion Plasmas, Varenna, 1985* (CEC, Luxembourg, 1986), Vol. 2, p. 531.
12. S. V. Konovalov, A. B. Mikhailovskii, V. S. Tsypin, *et al.*, Phys. Lett. A **318**, 429 (2003).
13. S. V. Konovalov, A. B. Mikhailovskii, M. S. Shirokov, and V. S. Tsypin, Plasma Phys. Controlled Fusion **44**, 579 (2002).
14. A. B. Mikhailovskii, M. S. Shirokov, V. S. Tsypin, *et al.*, Phys. Plasmas **10**, 3975 (2003).
15. S. V. Konovalov, A. B. Mikhailovskii, M. S. Shirokov, and V. S. Tsypin, Plasma Phys. Controlled Fusion **44**, L51 (2002).

Translated by S. Konovalov

Doklady Physics, Vol. 49, No. 7, 2004, pp. 409–410. Translated from Doklady Akademii Nauk, Vol. 397, No. 2, 2004, pp. 191–192.

PHYSICS

Jumps of the Contact-Potential Difference in a Magnetic Field and the Electron Energy Spectrum of Superlattices

V. N. Lutskiĭ

Presented by Academician Yu.V. Gulyaev March 11, 2004

Received March 11, 2004

In this paper, certain features of the behavior of the contact-potential difference in systems containing superlattices in a quantizing magnetic field are discussed. Some possibilities of investigating the electron energy spectrum of superlattices by analyzing the contact-potential difference are outlined. We show how features of the contact-potential difference can be used to determine the microscopic parameters of superlattices, such as the widths of allowed and forbidden minibands, cyclotron effective mass, and electron concentration.

Let us analyze a one-dimensional semiconductor superlattice with period d in a transverse quantizing magnetic field. The field is so strong that the energy spectrum of the semiconductor has gaps; i.e., the distance between Landau levels is larger than the widths Δ_i of allowed energy minibands ($\hbar\omega_c > \Delta_i$, where $\hbar$ is Planck's constant and ω_c is the cyclotron frequency). We also assume that, in the system under consideration, the number of particles is constant (e.g., it is a degenerate doped semiconductor), whereas temperature T is so low that $kT \ll \varepsilon_{gi}, \Delta_i$ (k is the Boltzmann constant and ε_{gi} is the width of forbidden minibands).

When the magnetic field varies, a series of metal–dielectric transitions must occur in such a system [1]. For each miniband, the number N of states per unit volume (miniband capacity) depends on the magnetic field H as

$$N = eH/2\pi\hbar cd,$$

where c is the speed of light. Therefore, when the total (in all minibands) density n of electric-current carriers is fixed, the field variation changes the filling of the last miniband. In this case, the Fermi level also changes smoothly. For the field values

$$H = H_s = \frac{2\pi\hbar cnd}{es}, \text{ where } s = 1, 2, \ldots,$$

the total concentration of current carriers is divisible by the capacity N of each miniband. In other words, the last populated miniband is filled (or depleted) as a whole, which results in a series of metal–dielectric transitions. The transitions occur with the period

$$\Delta\left(\frac{1}{H}\right) = \frac{e}{2\pi\hbar cnd}$$

in the inverse magnetic field $\Delta\left(\frac{1}{H}\right)$. When the magnetic field reaches values $H = H_s$, the Fermi level jumps from one miniband to another. In correlation with the (smooth or stepwise) variation of the Fermi level in dependence on the magnetic field, the work function of the superlattice and, therefore, the contact-potential difference of the system containing the superlattice change similarly.

We now discuss the behavior of the contact-potential difference under the above conditions. Let us analyze the contact-potential difference between the object being studied and a material whose electron spectrum (including the Fermi level) is weakly sensitive to the variation of the magnetic field (massive metal piece with large effective mass, insufficient structural perfection, etc.). In this case, all features of the contact-potential difference upon magnetic-field variations are associated with the shift of the Fermi level in the superlattice being studied. Then, the jumps of the Fermi level at the field values $H = H_s$ are directly manifested in the jumps of the contact-potential difference, and smooth variation of the Fermi level, in the smooth variation of the contact-potential difference.

For $d = 50$ Å and $n = 5 \times 10^{17}$ cm^{-3}, we obtain the estimate $H_1 = 9.8$ T.

Institute of Radio Engineering and Electronics, Russian Academy of Sciences, ul. Mokhovaya 11, Moscow, 103907 Russia
e-mail: lutskii@kmail.ru, irma@direct.ru

1028-3358/04/4907-0409$26.00

Using the measured jump of the contact-potential difference, one can immediately determine the width ε_{gi} of the corresponding forbidden miniband.

As is easy to understand, the change of the smooth part of the contact-potential difference as a function of the magnetic field between two successive jumps yields the width Δ_i of the corresponding allowed miniband. At the same time, the measurement of the jump repetition period in the inverse magnetic field makes it possible to find the product *nd* (i.e., to determine the electron concentration *n* using the *d* value known from technology).

The determination of the above quantities, including the periodicity of jumps, is independent of which minibands are neighboring. For intermediate and strong fields, these minibands are separated by gaps $\sim\hbar\omega_c$ and $\varepsilon_{i+1} - \varepsilon_i$, respectively.

Depending on which minibands are neighboring for chosen values of *H* and *d*, the quantity $[\varepsilon_{gi} + \frac{1}{2}(\Delta_i + \Delta_{i+1})]$ (for $\varepsilon_{gi} > \Delta_i$) yields the distance between either dimensional levels or Landau levels (as was indicated above, the quantities ε_{gi} and Δ_i are directly determined from measurements of the contact-potential difference). In the latter case, this quantity allows us to evaluate the cyclotron effective mass.

It is naturally assumed that the pinning of the Fermi level on the surface, as well as localized states in gaps between minibands, is absent.

The behavior of the contact-potential difference of a separate film under similar conditions was discussed previously in [2].

It is also worth noting that the use of oscillations of the contact-potential difference in massive metal pieces in a quantizing magnetic field for determination of the variation of the chemical potential was discussed in [3]. In the case of low-dimensional systems, effects of variation of the contact-potential difference are much more informative and pronounced.

ACKNOWLEDGMENTS

I am grateful to Yu.I. Balkareĭ, V.G. Baru, V.A. Volkov, and A.L. Musatov for stimulating discussions.

REFERENCES

1. V. N. Lutskiĭ, M. I. Kaganov, and A. Ya. Shik, Zh. Éksp. Teor. Fiz. **92**, 721 (1987) [Sov. Phys. JETP **65**, 406 (1987)].
2. V. N. Lutskiĭ, Radiotekh. Élektron. (Moscow) **45**, 873 (2000).
3. M. I. Kaganov, I. M. Lifshits, and K. D. Sinel'nikov, Zh. Éksp. Teor. Fiz. **32**, 605 (1957).

Translated by G. Merzon

Doklady Physics, Vol. 49, No. 7, 2004, pp. 411–414. Translated from Doklady Akademii Nauk, Vol. 397, No. 1, 2004, pp. 45–48.

TECHNICAL PHYSICS

Hyperspectral Remote Sounding of the Ground

Corresponding Member of the RAS S. P. Nepobedimyĭ, I. D. Rodionov, D. V. Vorontsov, A. G. Orlov, S. K. Kalashnikov, A. P. Kalinin*, M. Yu. Ovchinnikov, A. I. Rodionov, I. B. Shilov, V. N. Lyubimov, and A. F. Osipov

Received March 4, 2004

INTRODUCTION

We describe the first Russian aviation hyperspectrometer for gas pipelines (ASMG-1) developed and produced at the Scientific and Research Center Reagent in collaboration with a number of institutes of the Russian Academy of Sciences (Keldysh Institute of Applied Mathematics, Semenov Institute of Chemical Physics, Institute for Problems in Oil Processing, Institute for Problems in Mechanics) and aerospace-industry enterprises (NIIEM, Istra, Moscow oblast and TsSKB Progress, Samara).

Hyperspectral measurements in the optical band 0.3–2.5 μm are aimed at the remote sounding of the ground to identify objects and materials on the ground from aircraft, helicopters, and spacecraft. Hyperspectral measurements are measurements in the range from several hundreds to a thousand spectral channels. In contrast to widely used path spectrometers, a hyperspectrometer simultaneously measures the spectral and spatial coordinates. Numerous papers published in Proceedings of the International Society for Optical Engineering (SPIE, see, e.g., [1]) show that hyperspectral technology is now under intensive worldwide development.

The identification of objects and materials by hyperspectral measurements is based on the capabilities of these objects and materials to absorb and reflect light. The proposed method is fundamentally based on the one-to-one correspondence between the detected hyperspectral signal reflected from a surface and composition of this surface. For the illumination of the ground, solar radiation can be used in daytime, and lunar and stellar radiation, at night. The maximum of illumination radiation lies in the visible band, and the band 0.3–2.5 μm has optically transparent windows for the clean atmosphere.

Keldysh Institute of Applied Mathematics, Russian Academy of Sciences, Miusskaya pl. 4, Moscow, 125047 Russia

** e-mail: kalinin@ipmnet.ru, akalinin@reagent-rdc.ru*

The dependence of the intensity of radiation reflected from the ground on the spatial coordinate of a ground point, wavelength λ of detected radiation, and the components of the polarization of reflected radiation are measured. Due to the high sensitivity of the reflection coefficients of various objects to the frequency and polarization of illumination radiation, the hyperspectral method is exceptional among other methods of studying the ground. Hyperspectral data are particularly useful for solving complex problems of detecting small objects, identifying the composition of ground-based objects and processes occurring in the ground, distinguishing differences between close classes of objects, estimating biochemical and geophysical parameters, etc. Only hyperspectral measurements can reveal small spectral differences between individual elements of the ground and provide indicators of objects of interest and processes on the ground.

The transition from traditional multidomain survey to hyperspectral survey increases the amount of information and provides the new unique quality of hyperspectral data. However, these new data can be extracted only by substantially improved methods for processing information.

The basic approach for processing multidomain data consisting of 3–5 spectral lines in available devices and up to 20–30 lines in future systems is the 2D spatial processing of only the spectral band that is most informative among the measured lines for an applied problem under consideration. Hyperspectral data allow analysis of an object that has no characteristic isolated spectral lines by processing the entire measured spectrum. Due to this property, the hyperspectral method of remote sounding differs qualitatively from the multidomain method.

Since the number of detected spectral channels is large, and the above identification problems are complex, it is necessary to ensure automatic or semiautomatic computer processing of hyperspectral information and its interpretation. The basic notion of hyperspectral survey is a hypercube, i.e., the set of intensities of radiation reflected from the 2D ground surface conditionally divided into image elements, pixels. In addi-

1028-3358/04/4907-0411$26.00

tion to two standard metric coordinates, each pixel includes the spectral coordinate, providing the 3D data space. The discrete polarization coordinate is also added. Thus, measured data are values of a function specified in the multidimensional space including continuous and discrete coordinates.

DESCRIPTION OF THE HYPERSPECTROMETER

The created hyperspectrometer [2, 3] consists of modules for various frequency bands. These modules operate synchronously in the field of view and frame survey, are combined in the unified onboard system,

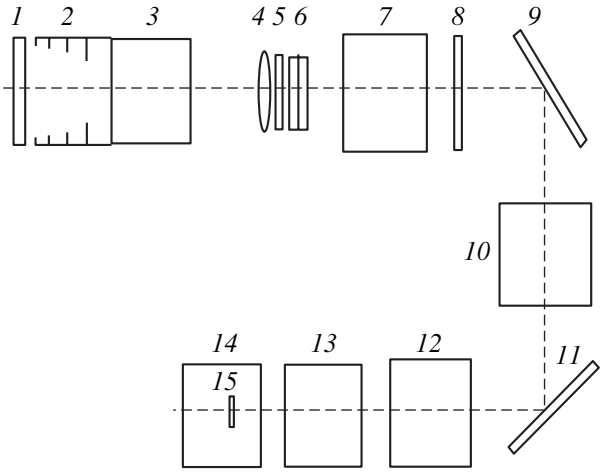

Fig. 1. Hyperspectrometer layout: (*1*) window, (*2*) blend, (*3*) input objective, (*4*) collector, (*5*) input slit, (*6*) optical filter, (*7*) collimator, (*8*) polarizer, (*9*) diffraction grating, (*10*) camera objective, (*11*) deviating mirror, (*12*) image intensifier, (*13*) projection objective, (*14*) video camera without an objective, (*15*) CCD matrix.

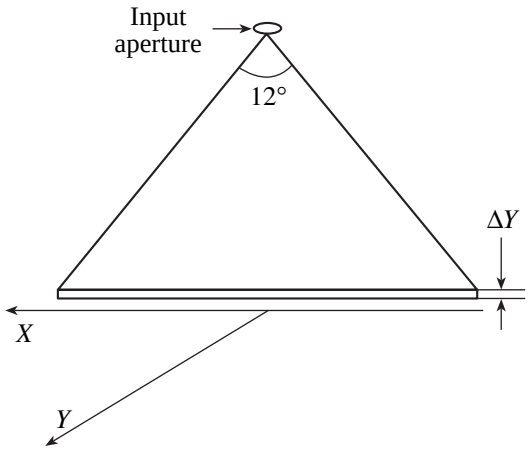

Fig. 2. Ground belt projected on the input of the image intensifier. The belt width in the *Y* coordinate is determined by an angle of 1° and flight altitude.

and cover the ultraviolet band $\lambda \sim 0.3$–0.4 μm, as well as the first and second visible bands $\lambda \sim 0.43$–0.7 and 0.66–0.86 μm, respectively. A module for the infrared band $\lambda \sim 0.85$–2.5 μm is under production. Data from all modules are united when processing, and the overall spectral function is finally obtained over the entire frequency range under investigation. All modules have the same construction, and Fig. 1 shows the layout of one of them.

An input aperture with a diameter of 3 cm and instantaneous field of view of $12° \times 1'$ of each module provides the formation of an image of the ground belt, whose sizes are determined by the flight altitude of an aircraft, helicopter, or spacecraft, on the input of an image intensifier (see Fig. 2).

In the device under consideration, a 1D plane diffraction grating is used. Its feature is the conservation of the spatial distribution of light flux over one of the coordinates and scanning of the intensity of a spectral line over another coordinate with deflection depending on the line wavelength. The deflection angle of the spectral line is proportional to the wavelength, which allows the scanning of a plane flux over the angular coordinate as a function of the wavelength.

The diffraction grating and image intensifier form an image on the matrix of a charge-coupled device (CCD). One axis of the image shows the *X* coordinate of a narrow ground belt (Fig. 2), the second axis shows the wavelength λ of radiation reflected from the ground, and the charge of each matrix element (pixel) presents intensity determining the spectral density of the wavelength. Thus, a set of the spectral functions of radiation reflected from the ground is obtained on the CCD matrix as a function of the *X* coordinate. Since an aircraft, helicopter, or spacecraft with the hyperspectrometer moves along the *Y* coordinate (Fig. 2), various belts of the ground are studied step by step.

In a flight experiment, a visual signal received from a black-and-white video camera of the hyperspectrometer is recorded on a videotape recorder with a vertical-sweep frequency of 25 Hz. In addition to video signals, synchronization markers from the visual-observation camera are recorded in the audio channel. They ensure the common time reference for all devices of the complex. Then, records are processed in a laboratory by reproducing a survey section of interest on a studio videotape recorder and digitalizing it by means of a video capture card.

To identify a hyperspectral image, it is necessary to compare the spectral functions measured for the image element under investigation and the spectral functions of known substances of the ground; i.e., the spectral database of substances is necessary. To this end, the spectral function of solar light reflected from the surfaces of known substances for analysis, e.g., bog surface, is determined.

METHODS OF INTERPRETATION OF HYPERSPECTRAL IMAGES

Hyperspectral images are interpreted by two methods. First, if each element of a hyperspectral image corresponds to one substance, the correlation method is used. Second, if each element of hyperspectral image corresponds to a set of substances, the subpixel method is used.

In the correlation method, among the reference components, a substance with the spectral function closest to the spectral function of each point of the hyperspectral image is selected. Mathematically, this method is a particular case of the more general subpixel-transformation method [2, 4]. The latter method is based on the scalar product of two vectors in multidimensional space and may be used to determine the contribution from each element of the database if the basis formed by this database is orthogonal. The algorithmic simplicity is undoubtedly a merit of the correlation method. It is stable against noise associated with illumination and various nonlinearities of equipment. The much lower information content of the pattern obtained by processing hyperspectral data is a drawback of this method compared to the subpixel method described below.

All ground materials are usually mixtures of several substances at all measurement scales. Therefore, the spectral function of a surface image element is a composition of the spectral functions of several reference components. This property is inconsistent with the correlation method, implying the presence of only one component in the image element. Approximating the spectral function of each image element by a linear combination of limited reference spectral samples, one can estimate the composition of the pixel image by the least squares method [4].

The linear decomposition model is used in our transformation. This model implies the approximation of each element of the hyperspectral image by a linear combination of the reference components with the corresponding weights.

EXPERIMENTAL RESULTS

As an example of the hyperspectral remote sounding of the ground and mathematical processing of hyperspectral image data by the correlation method, we consider the results of survey of the Yamburg gas field from an IL-20 aircraft (the expedition was organized and headed by N.N. Khrenov) [5]. Figure 3 exemplifies the subpixel identification of a domain with a road and pipeline. The correspondence of shades to the reference elements is shown. The presence of several kinds of substances of the same nature (e.g., two sorts of sand) means that these surfaces look like sand but have different spectral functions. When processing on a computer, various colors are used for elements, and such color drawings were exemplified in [1]. In Fig. 3, *1* is the ground road, *2* is the gas pipeline coming to the surface, and *3* is the removal of sand from the gas pipeline route that is responsible for the denudation of the gas pipeline.

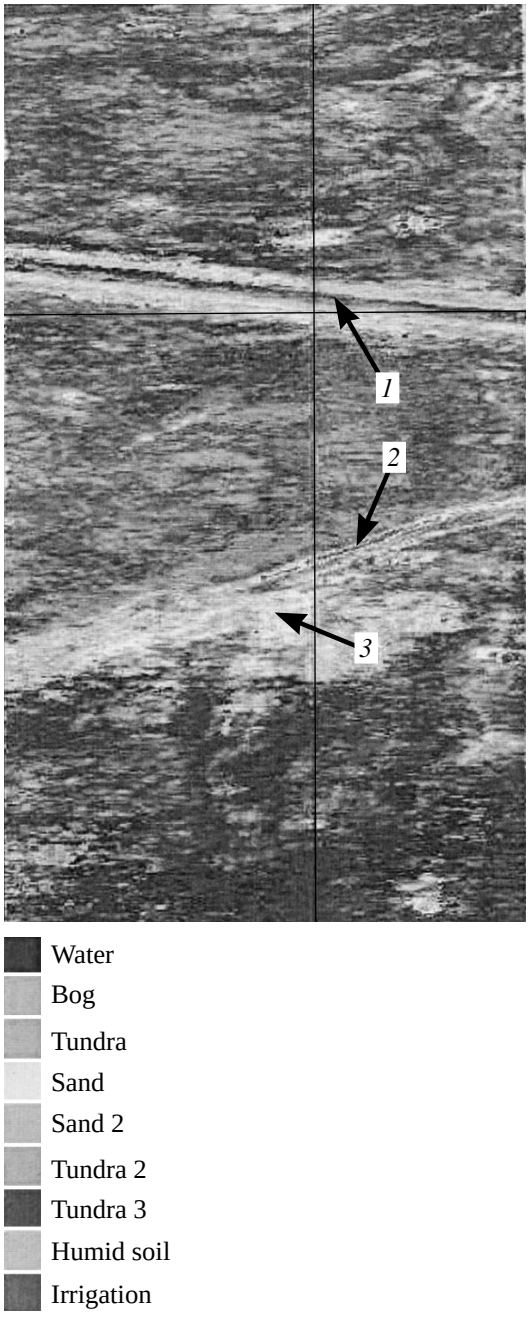

Fig. 3. Example of the subpixel interpretation of a domain with a road and pipeline: *1* is the ground road, *2* is the gas pipeline coming to the surface, and *3* is the removal of sand from the gas pipeline route that is responsible for the denudation of the gas pipeline.

On the basis of the results, the space hyperspectral equipment is developed for the remote sounding of the ground (Resurs 01 and Vulkan-Astrogon satellites of

the Vulkan space system). This development is supported by the Russian Federal Space Program [5].

Thus, the first Russian hyperspectrometer has been produced. The procedure of processing and interpretation of hyperspectral data has been developed. Field tests of the hyperspectrometer were carried out from a helicopter and aircraft. The above example of the interpretation of hyperspectral photos shows both the efficiency of the subpixel method of interpreting remote-sounding photos of the ground and the fundamental novelty of the results.

REFERENCES

1. D. V. Vorontsov, A. G. Orlov, A. P. Kalinin, *et al.*, Preprint No. 702, IPM RAN (Institute for Problems in Mechanics, Russian Academy of Sciences, Moscow, 2002).
2. D. V. Vorontsov, A. G. Orlov, A. P. Kalinin, *et al.*, Preprint No. 703, IPM RAN (Institute for Problems in Mechanics, Russian Academy of Sciences, Moscow, 2002).
3. D. Manolakis, C. Siracusa, and G. Shaw, IEEE Trans. Geosci. Remote Sens. **39**, 1392 (2001).
4. N. N. Khrenov, A. N. Dmitrievskiĭ, A. G. Ananenkov, *et al.*, Nauka Tekhnika Gaz. Prom., No. 2, 37 (2001).
5. L. Makridenko, R. Salikhov, M. Ovchinnikov, *et al.*, in *Extended Abstracts of the 4th International IAA Symposium "Small Satellites for Earth Observation," Berlin, 2003*, pp. 141–144.

Translated by R. Tyapaev

Doklady Physics, Vol. 49, No. 7, 2004, pp. 415–418. Translated from Doklady Akademii Nauk, Vol. 397, No. 2, 2004, pp. 193–197.

TECHNICAL PHYSICS

Correlation between the Copper Structure and Temperature–Rate Parameters of Pressure-Induced Shear Deformation

M. V. Degtyarev, T. I. Chashchukhina, M. Yu. Romanova, and L. M. Voronova*

Presented by Academician V.M. Schastlivtsev January 15, 2004

Received February 18, 2004

Interest in materials with nano- and submicrocrystalline structures stimulates the development of methods of intense deformation impact. Due to its high plasticity, copper is a model material for testing these techniques, and the evolution of the copper structure under large plastic deformation was studied in many works [1–5].

Change in the structure and properties of copper under large deformation differs from that in iron alloys. Indeed, the start temperature of copper recrystallization varies nonmonotonically upon an increase in the number of cycles of equal-channel angular pressing [1], a few large recrystallized grains are present in the structure immediately after equal-channel angular pressing [2], and the recrystallization process upon further heating is anomalous [1]. The same anomalous growth of a grain is observed upon heating copper undergoing pressure-induced shear deformation [3]. These effects can be attributed to the development of dynamic recrystallization whose structural indications are found upon both pressure-induced shear deformation of copper with $e > 5$ [4] and torsion of cylindrical copper specimens at room temperature [5].

Nevertheless, many authors disregard dynamic recrystallization and analyze the evolution of the copper structure similarly to the case of cold deformation [1, 3].

Dynamic recrystallization shows that deformation under these conditions may be treated as hot deformation. In this case, the material structure is determined by the temperature and rate of deformation rather than by its degree. The joint effect of the temperature and rate of deformation is represented by the Zener–Hollomon parameter [6]. The maps of structure states presenting the processes of structure formation for various Zener–Hollomon parameters upon hot deformation of fcc single crystals were published in [7]. Thus, this work is aimed at determining the correspondence between the copper structure in the pressure-induced shear-deformation process at room temperature and the temperature–rate conditions of deformation.

Specimens of 99.99% copper with a diameter of 5 mm and thickness of 0.3 mm were deformed through shear induced by a pressure of 6 GPa. The anvil rotation angle was varied from 15° to 15 revolutions. It was assumed that each deformed specimen first undergoes structure changes similar to those occurring in specimens deformed with lower anvil rotation angles, and differences arise upon an increase of the degree of deformation in further rotation. The degree of deformation was calculated by the formula

$$e = \ln\left(1 + \frac{\varphi R}{h_{iR}^2}\right)^{1/2} + \ln\frac{h_0}{h_{iR}}, \quad (1)$$

where φ is the anvil rotation angle and h_0 and h_{iR} are the thicknesses of the specimen before and after deformation at distance R from the center, respectively.

The deformation rate is determined by the expression

$$\dot{e} = \frac{\Delta e}{\Delta\tau}, \quad (2)$$

where Δe is the degree of deformation at which the structure changes compared to a specimen deformed with a lower anvil rotation angle and $\Delta\tau$ measured in seconds is the time in which the corresponding degree of deformation is reached. The Zener–Hollomon parameter is determined as [6, 7]

$$\ln Z = \ln\dot{e} + \frac{\Delta H}{RT}, \quad (3)$$

where $\Delta H = 107$ kJ/mol is the energy of the activation of grain growth in copper [3]. According to calculations made in [8] and experimental data, the temperature of the specimen upon pressure-induced shear is assumed

Institute of Metal Physics, Ural Division, Russian Academy of Sciences, ul. S. Kovalevskoĭ 18, Yekaterinburg, 620219 Russia

** e-mail: highpress@ipm.uran.ru*

1028-3358/04/4907-0415$26.00 © 2004 MAIK “Nauka/Interperiodica”

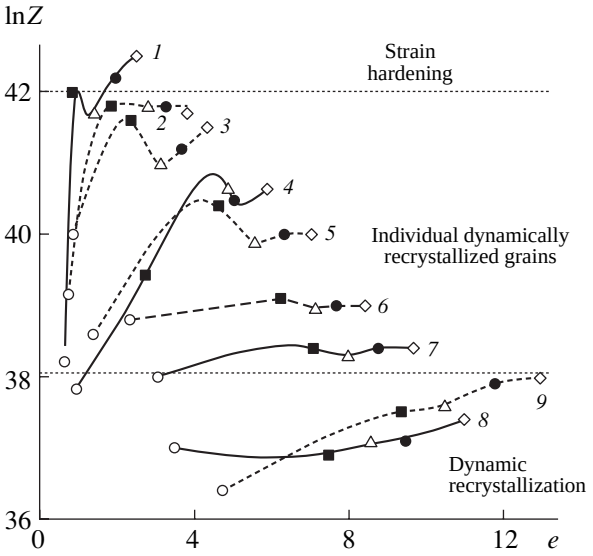

Fig. 1. Zener–Hollomon parameter ln$Z$ along the radius of specimens deformed with an anvil rotation angle of (*1*) 15°, (*2*) 45°, (*3*) 60°, and (*4*) 180° and (*5*) 1, (*6*) 2, (*7*) 5, (*8*) 10, (*9*) 15 revolutions for R = (squares) 0.5, (triangles) 1.0, (closed circles) 1.5, and (diamonds) 2.0 mm; open circles correspond to the center of the specimen.

to be close to room temperature (T = 300 K). For a series of specimens deformed with the same anvil rotation angle, the spread of ln$Z$ values that was associated with the reproducibility of experimental data was no more than 0.5.

The structure was analyzed at distances of 0.5 and 1.5 mm from the specimen center. The size of structure components was determined on the electron microscopic images with an error of less than 10%. The histograms of the size distribution of the structure components were plotted by using the results of more than 200 measurements.

It is known [7] that the range $34 < \ln Z < 38$ in single crystals of fcc alloys corresponds to developed dynamic recrystallization. In the range $38 < \ln Z < 42$, the volume fraction of the recrystallized structure decreases, and dynamic recrystallization is not developed for $\ln Z > 42$. Dynamic recrystallization is absent for large ln$Z$ values, because the deformation time is insufficient for the formation of a nucleus that can grow. Dynamic recrystallization does not occur for $\ln Z < 34$, because the driving force of recrystallization is insufficient due to the dynamic return.

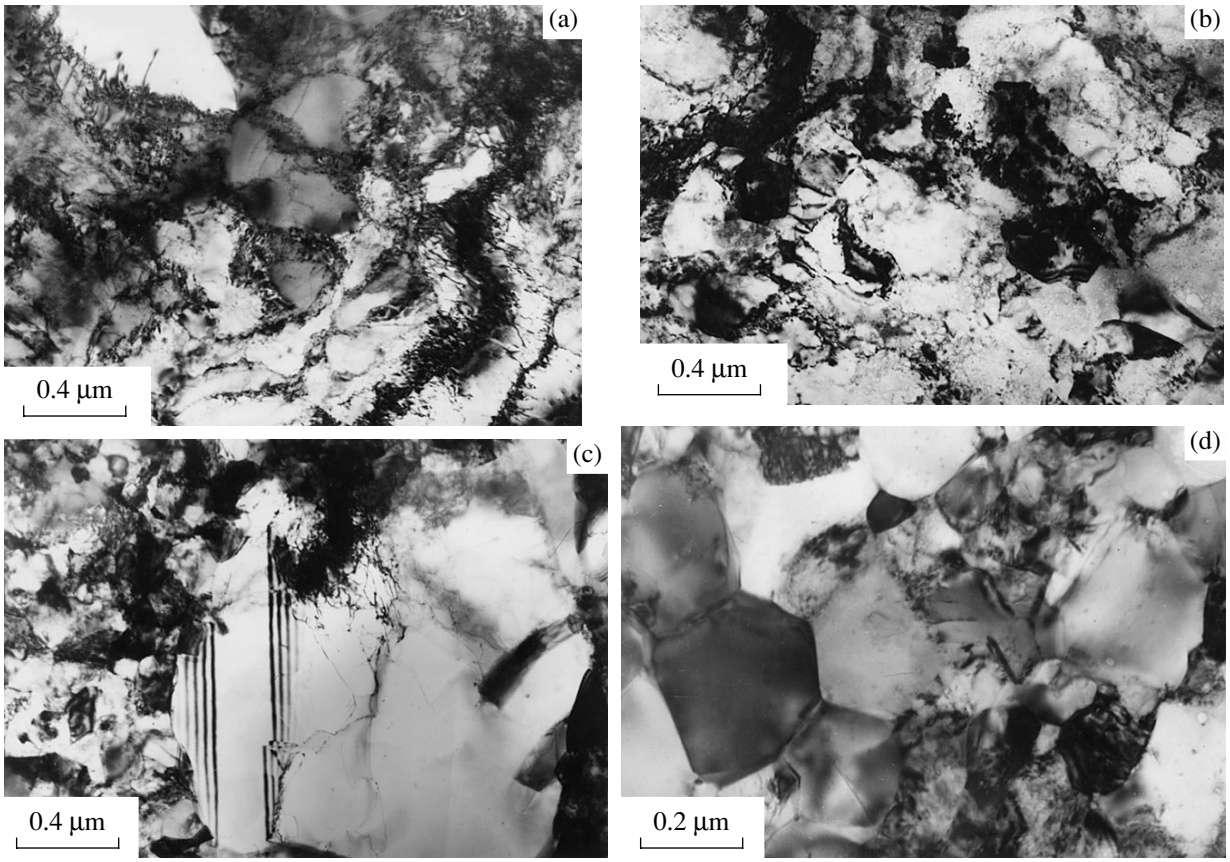

Fig. 2. Microstructure of a copper specimen deformed with an anvil rotation angle of (a) 15°, (b) 45°, (c) 180°, and (d) 10 revolutions for R = (a, c, d) 1.5 and (b) 0.5 mm.

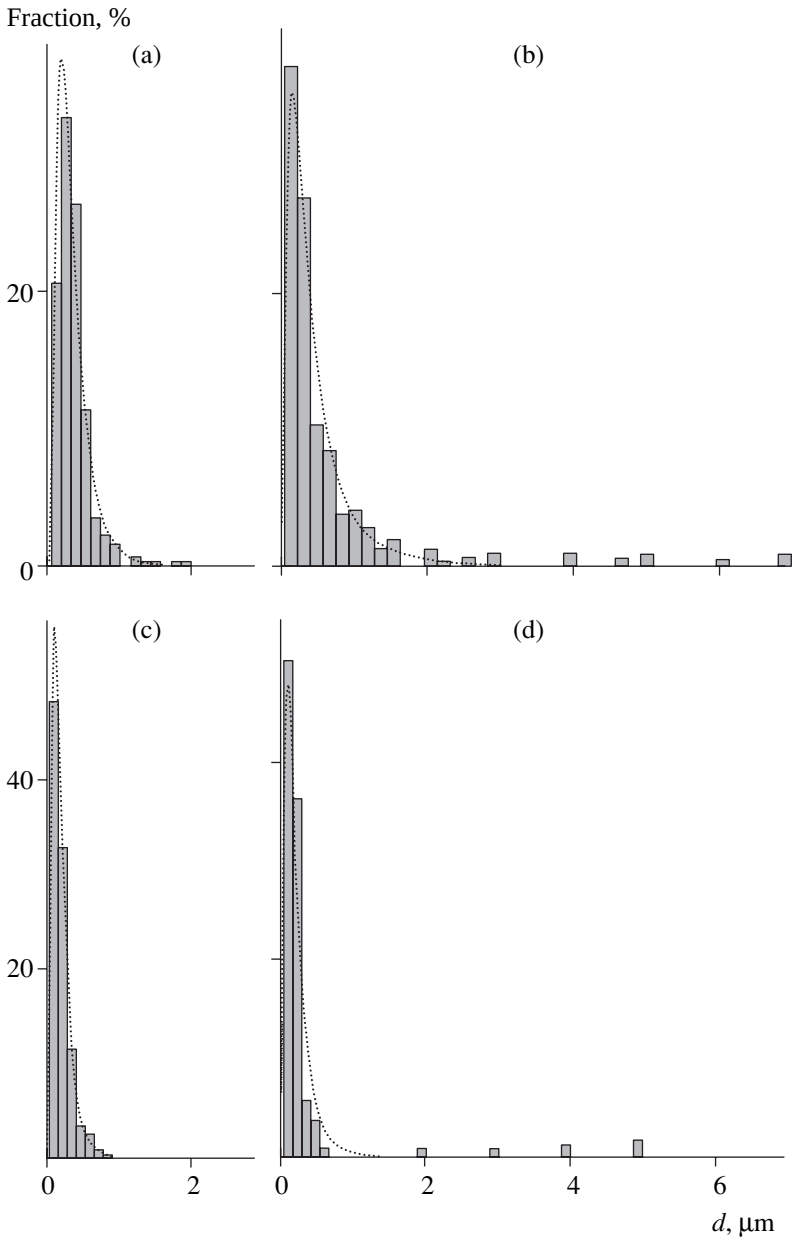

Fig. 3. Histograms of the size distribution of the structure components of a copper specimen deformed with an anvil rotation angle of (a) 45° and (b) 5, (c) 10, and (d) 15 revolutions for $R = 1.5$ mm.

The Zener–Hollomon parameter varies in the range $36 < \ln Z < 43$ upon pressure-induced shear deformation of copper at room temperature (Fig. 1). The strain rate varies with the distance from the center of a specimen undergoing pressure-induced shear. In iron and construction steels, this variation of the strain rate does not change the relaxation mechanism, and the structural parameters remain the same at different radii, where the same degree of deformation is reached in different anvil revolution numbers [9]. In copper, the Zener–Hollomon parameter for the same degree of deformation depends on the strain rate. This property can be responsible for the difference not only in the parameter but also in the structure type.

As is seen in Fig. 1, after the rotation of the anvil by 15°, strain hardening should be expected in a specimen at distances no less than 1.5 mm from the center. Dynamic recrystallization should be expected over the entire specimen after deformation by 10 and 15 revolutions. The structure of other deformed specimens must be partially dynamically recrystallized.

The termination of deformation at high temperature leads to post-dynamic recrystallization whose development is suppressed by fast cooling to room temperature. In this study, room temperature coincides with the deformation temperature. Therefore, it is impossible to avoid post-dynamic recrystallization, and the structure

is formed both in the deformation process and after its termination.

After the rotation of the anvil by 15°, a cellular structure is formed at a distance of 1.5 mm ($e = 2$) from the specimen center (Fig. 2a). In addition to dislocation cells, recrystallization nuclei whose boundaries have the characteristic band contrast are observed at a distance of 0.5 mm from the center for the same degree of deformation in a specimen deformed by 45° (Fig. 2b). According to Fig. 1, $\ln Z$ values for these specimens after the same deformation correspond to different regions of structure states. Thus, dynamic recrystallization in deformed copper specimens begins with the parameter $\ln Z < 42$ when the degree of deformation $e = 2$ is reached.

Large recrystallized grains containing annealing twins and sections with an increased strength of defects are observed in the structure after one revolution of the anvil (Fig. 2c). The presence of riveting sections testifies to the formation of a grain in the dynamic recrystallization process. The presence of annealing twins indicates post-dynamic recrystallization that leads to the coarsening of certain dynamically recrystallized grains.

With an increase in the degree of deformation in specimens from 45° to 5 revolutions, the fraction of the unrecrystallized structure decreases. The size of large structure components is more than tripled (Fig. 3). In this case, the parameter $\ln Z$ decreases (Fig. 1).

After deformation by ten revolutions, the distribution maximum is shifted to lower sizes and narrowed more than half (Fig. 3c). The size of the largest grain is almost an order of magnitude smaller than that after five revolutions. In this case, $\ln Z = 37.3 \pm 0.2$; i.e., it corresponds to the developed dynamic recrystallization. Nevertheless, the structure is inhomogeneous (Fig. 2d). Domains formed by geometrically perfect grains alternate with domains that are occupied by grains with a high density of defects and contain individual statically recrystallized grains of an irregular shape. The geometrical and dislocation inhomogeneities of grains can explain their different capabilities to heating-induced growth.

The specimen deformed by 15 revolutions passes the stage of the formation of a size-homogeneous structure (10 revolutions). Then, due to a change in the actual strain rate ($\ln Z$ increases to 38.0 ± 0.1), deformation continues in the region of incomplete dynamic recrystallization. As a result, the parameters of the distribution maximum do not change, but large (up to 5 μm) post-dynamically recrystallized grains appear in the structure (Fig. 3d). Their formation can be attributed to the appearance of structure microvolumes that are not involved in dynamic recrystallization and characterized by high accumulated energy. Thus, the completely dynamically recrystallized structure is formed in copper for $\ln Z < 38$.

Hardness is an important characteristic of a material undergoing pressure-induced shear deformation. In materials where plastic deformation is accompanied by work hardening, hardness correlates with the size of the structural components and provides information on the change of the stages of structure formation [9]. In this experiment, hardness increases from 1 to 1.8 GPa when a copper specimen is deformed up to $e = 2$. Then, up to $e = 8$, hardness remains constant and is characterized by wide spread (±10%). With the further increase in the degree of deformation, hardness decreases. Hardness cannot characterize the structure state of a material under developed dynamic and post-dynamic recrystallization.

The pressure-induced shear deformation of copper up to $e = 2$ leads to strain hardening. With an increase in the degree of deformation, thermally activated processes begin to affect the formation of the structure. Dynamic recrystallization is developed, and the further evolution of the structure is determined by the temperature-compensated strain rate.

ACKNOWLEDGMENTS

This work was supported by the Council of the President of the Russian Federation for Support of Young Russian Scientists and Leading Scientific Schools (project no. NSh-778.2003.3) and the program "Fundamental Problems of Physics and Chemistry of Nanosystems and Nanomaterials," the Presidium of the Russian Academy of Sciences (project no. 7).

REFERENCES

1. V. N. Chuvil'deev, V. I. Kopylov, A. V. Nokhrin, *et al.*, Materialovedenie, No. 4, 9 (2003).
2. V. I. Kopylov, I. M. Makarov, E. V. Nesterova, and V. V. Rybin, Vopr. Materialovedeniya, No. 1 (29), 273 (2002).
3. N. M. Amirkhanov, R. K. Islamgaliev, and R. Z. Valiev, Fiz. Met. Metalloved. **86** (3), 99 (1998).
4. N. A. Smirnova, V. I. Levit, V. P. Pilyugin, *et al.*, Fiz. Met. Metalloved. **61**, 1170 (1986).
5. V. M. Bykov, V. A. Likhachev, Yu. A. Nikonov, *et al.*, Fiz. Met. Metalloved. **45**, 163 (1978).
6. M. L. Bernshteĭn, V. A. Zaĭmovskiĭ, and L. M. Kaputkina, *Thermomechanical Treatment of Steel* (Metallurgiya, Moscow, 1983).
7. V. I. Levit and M. A. Smirnov, *High-Temperature Thermomechanical Treatment of Austenite Steels and Alloys* (ChGTU, Chelyabinsk, 1995).
8. V. P. Pilyugin, Candidate's Dissertation (Institute of Metal Physics, Ural Division, Russian Academy of Sciences, Yekaterinburg, 1993).
9. M. V. Degtyarev, L. M. Voronova, and T. I. Chashchukhina, Metally, No. 3, 53 (2003).

Translated by R. Tyapaev

Doklady Physics, Vol. 49, No. 7, 2004, pp. 419–421. Translated from Doklady Akademii Nauk, Vol. 397, No. 2, 2004, pp. 198–200.

TECHNICAL PHYSICS

Radiation of Ultrawideband Pulses from a Coaxial Waveguide into an Open Space between Conducting Bodies

V. I. Koroza and M. N. Golikov*

Presented by Academician V.N. Mikhaĭlov February 10, 2004

Received February 10, 2004

The rapid development of the technique of ultrawideband electromagnetic pulses [1, 2] provides new problems for investigations. One of them is the elaboration of standard devices for metrological maintenance of works with ultrawideband electromagnetic pulses with subnanosecond time parameters. Facilities such as those schematically shown in Fig. 1 are convenient for these purposes. The work of these facilities is based on the calibration of electromagnetic field sensors in the space B between conducting bodies A (with plane boundary $z = 0$) and C [body of revolution around the Z axis with the boundary $r = a(z)$]. The field of ultrawideband electromagnetic pulses in space B is excited through a coaxial waveguide by means of initial-structure pulses of transverse electromagnetic waves with a given initial ($t = 0$) form $\varphi(z)$. The metallic bodies A and C, as well as the material of the waveguide walls, are treated as ideally conducting.

According to general requirements to standard devices, the accuracy of electrodynamic calculations of the pulse excitation in the space B must be high and the accuracy of these calculations must be controlled. For these reasons, the frequency approach is inapplicable and new, more general, methods of calculations for such facilities must be developed. In this work, we show that the basic concept of the coupled-string method for calculating pulse processes in irregular closed transmission lines can be generalized and applied to irregular mixed-type lines including open sections (Fig. 1, $z > 0$) along with closed sections ($z < 0$). This method is based on the set of time-dependent waveguide equations [3] and was successfully tested on closed irregular lines [4, 5].

The set of time-dependent waveguide equations has the matrix form [3]

$$\frac{\partial}{\partial z}\left[G(z)\frac{\partial \mathbf{f}}{\partial z} + Q(z)\mathbf{f}\right]$$
$$- Q^{\tau}(z)\frac{\partial \mathbf{f}}{\partial z} - P(z)\mathbf{f} - T(z)\frac{\partial^2 \mathbf{f}}{\partial t^2} = 0, \qquad (1)$$

where the z coordinate and time t are independent variables. The components $f_j(z, t)$ of the unknown column vector $\mathbf{f}(z, t)$ are the coefficients in the decomposition of the azimuthal magnetic-field component $H(\mathbf{r}_\perp, z, t)$, which is the only nonzero component in the case under consideration, in a certain given set of basis functions $\{e_j(\mathbf{r}_\perp, z)\}$:

$$H(\mathbf{r}_\perp, z, t) = \Sigma e_j(\mathbf{r}_\perp, z) f_j(z, t). \qquad (2)$$

The dimension $[N]$ of the column vector $\mathbf{f}(z, t)$ and the dimension $[N \times N]$ of the square matrix functions $\mathbf{G}(z)$

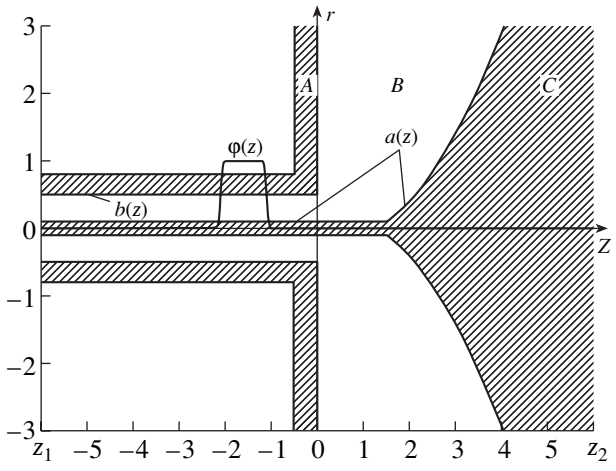

Fig. 1.

Institute of Strategic Stability,
Luganskaya ul. 9, Moscow, 115304 Russia
** e-mail: mikeng@mail.ru*

1028-3358/04/4907-0419$26.00 © 2004 MAIK “Nauka/Interperiodica”

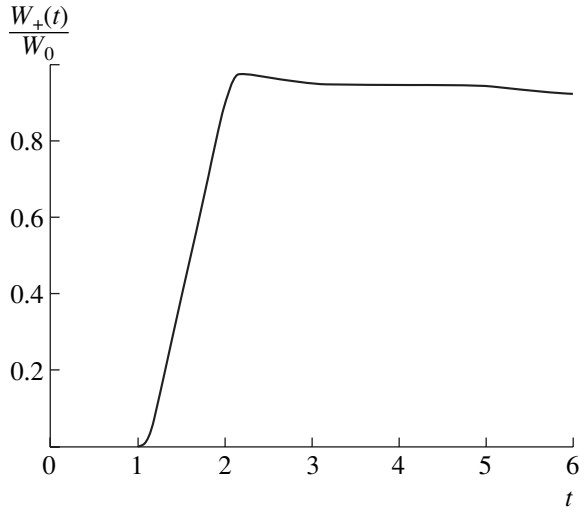

Fig. 2.

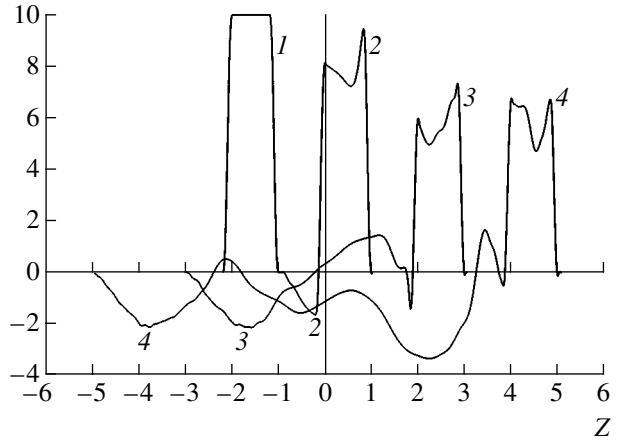

Fig. 3.

and $\mathbf{Q}(z)$, transposed matrix function $\mathbf{Q}^{\tau}(z)$, and matrix functions $\mathbf{P}(z)$ and $\mathbf{T}(z)$ in set (1) are determined by the number N of the terms taken into account in sum (2). These matrix functions are given by their matrix elements

$$G_{ns}(z) = \int\limits_{S(z)}\int \varepsilon^{-1} e_s e_n \, dS, \quad T_{ns}(z) = \int\limits_{S(z)}\int \mu e_s e_n \, dS,$$

$$Q_{ns}(z) = \int\limits_{S(z)}\int \varepsilon^{-1} (e_s)_z e_n \, dS, \tag{3}$$

$$P_{ns}(z) = \int\limits_{S(z)}\int \varepsilon^{-1}\{(e_s)_z (e_n)_z + r^{-2}(re_s)_r (re_n)_r\} dS,$$

where $S(z)$ are the plane cross sections of the channel that are orthogonal to the Z axis and the subscripts z and r stand for the differentiation with respect to these variables.

As the set $\{e_j(\mathbf{r}_\perp, z)\}$ in expansion (2), the field distribution functions in the coaxial line for the transverse electromagnetic wave ($j = 1$) and E_{0P} waves ($p = j - 1$, $j = 2, 3, \ldots$) are used for $z < 0$, and $e_j(\mathbf{r}_\perp, z) = \frac{1}{r^2} J_1\left(\frac{\nu_j a(z)}{r}\right)$, where $j = 1, 2, \ldots$, ν_j are the positive roots of the equation $J_0(x) = 0$ that are numbered in increasing order, and $J_0(x)$ and $J_1(x)$ are Bessel functions of the first kind, are used for $z > 0$. Here, the modes H_{0P} are disregarded, because they are absent by assumption at $t = 0$ and do not arise under the above conditions for $t > 0$.

Since the basis functions $e_j(\mathbf{r}_\perp, z)$ and, therefore, $\mathbf{f}(z, t)$ are discontinuous in the cross section $S(0)$, the definition of set (1) is completed at $z = 0$ by the conditions

$$A_- \frac{\partial \mathbf{f}_-}{\partial z} + B_- \mathbf{f}_- = A_+ \frac{\partial \mathbf{f}_+}{\partial z} + B_+ \mathbf{f}_+. \tag{4}$$

Here, $\frac{\partial \mathbf{f}_\pm}{\partial z}$ and $\mathbf{f}_\pm$ are the (+) right and (–) left values of $\frac{\partial \mathbf{f}}{\partial z}$ and $\mathbf{f}$ at $z = 0$. The dimensions of the unknown column vectors $\mathbf{f}_+$ and $\mathbf{f}_-$ are equal to, respectively, the numbers N_+ and N_- of terms taken into account in Eq. (2) for $z < 0$ and $z > 0$, respectively. The $(N_+ + N_-) \times N_+$ matrices A_+ and B_+ and the $(N_+ + N_-) \times N_-$ matrices A_- and B_- are determined by the requirements to the transverse components of fields in the cross section $z = z_0$, continuous condition for $r < b(0)$, and condition $E_r = 0$ for $r > b(0)$.

Equation (1) for a pulse with the initial ($t = 0$) structure of a transverse electromagnetic wave shown by the trapezoidal curve $\varphi(z)$ in Fig. 1 over the background of the channel configuration is numerically solved by applying a mixed (locally implicit) difference scheme with computational cell sizes $hz = 0.01$ and $ht = 0.004$. Real calculations are preformed with the parameters $a(z) \equiv a_0 = 0.1$, $b(z) \equiv b_0 = 0.5$, $\varepsilon = \mu = 1$, $N_- = 5$, and $N_+ = 15$.

Figure 2 shows the calculations of the forward-passing ($z > z_0$) fraction of energy $\frac{W_+(t)}{W_0}$ accumulated in the pulse, where W_0 is the total electromagnetic energy of the pulse and $W_+(t)$ is the fraction of this energy that is concentrated in the half-space $z > 0$. The shapes of the magnetic-field pulse calculated for $t =$ (*1*) 0, (*2*) 2, (*3*) 4, and (*4*) 6 are shown in Fig. 3. The error of calculations is estimated by the relative spread of the total electromagnetic energy accumulated in the pulse for various times t. Figure 4 shows the results obtained with the

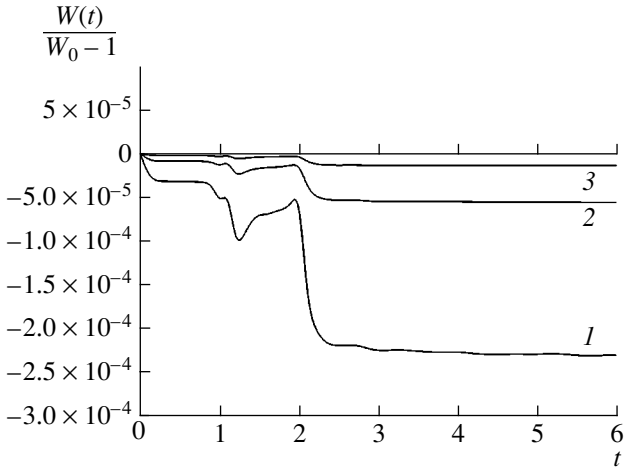

Fig. 4.

computational grid with the initial sizes hz = (*1*) 0.01, (*2*) 0.005, and (*3*) 0.0025 and ht = (*1*) 0.004, (*2*) 0.002, and (*3*) 0.001, respectively. The relative error for the computational grid with the initial sizes is no more than 2.5×10^{-4} and decreases when dividing each size.

Thus, it is shown that fast processes of qualitative restructurization of ultrawideband electromagnetic pulses passing through the junctions of coaxial waveguides with irregular open waveguides can be efficiently simulated and accurately calculated. The structure of pulses, which initially are transverse waves, partially reflected, and transformed to the longitudinal waves propagating transversely, changes immediately near the flange joint in a short time interval when the pulse passes near it.

REFERENCES

1. *Ultra-Wideband, Short-Pulse Electromagnetics 3*, Ed. by C. E. Baum, L. Carin, and A. P. Stone (Plenum, New York, 1997).
2. *Ultra-Wideband, Short-Pulse Electromagnetics 4*, Ed. by E. Heyman, B. Mandelbaum, and J. Shiloh (Plenum, New York, 1999).
3. V. I. Koroza, Pis'ma Zh. Tekh. Fiz. **22** (21), 6 (1996) [Tech. Phys. Lett. **22**, 865 (1996)].
4. V. I. Koroza and M. N. Golikov, Dokl. Akad. Nauk **393**, 191 (2003) [Dokl. Phys. **48**, 637 (2003)].
5. V. I. Koroza and M. N. Golikov, Radiotekh. Élektron. (Moscow) **49** (3), 292 (2004) [J. Commun. Technol. Electron. **49** (3), 267 (2004)].

Translated by R. Tyapaev

Doklady Physics, Vol. 49, No. 7, 2004, pp. 422–425. Translated from Doklady Akademii Nauk, Vol. 397, No. 3, 2004, pp. 330–333.

TECHNICAL PHYSICS

Mechanical Properties of High-Carbon Alloy Steel near the Phase-Transformation Temperature

É. I. Éstrin and B. M. Mogutnov*

Presented by Academician O.A. Bannykh February 19, 2004

Received February 26, 2004

Phase transformations accompanying plastic deformation can affect the deformation process and, therefore, the mechanical properties of a material [1, 2]. The trip effect—an increase in steel plasticity due to a martensitic transformation accompanying deformation—is the most well-known such effect (see, e.g., reviews [3, 4]). Phenomena caused by interaction between deformation and low-temperature (martensitic) transformations are quite well studied, and some of them are used in practice, e.g., in trip steels [4]. Interaction between deformation and transformations other than martensitic ones is less studied. In particular, whether or not an effect similar to the trip effect associated with martensitic transformations accompanies high-temperature transformations is an open question. At the same time, a nonmonotonic temperature dependence of the plastic properties of various steels was observed in several high-temperature mechanical tests in the region of phase transformations [1, 3, 5]. However, the origin of this phenomenon is still unclear.

In this work, the mechanical properties of high-carbon alloy steel in the ferrite–carbide and austenite–carbide states in the temperature range of the $\alpha \longleftrightarrow \gamma$ transformation is studied in order to determine the temperature dependence of these properties, to reveal the laws of interaction between plastic deformation and phase transformations, and to analyze the possibility that an effect similar to the trip effect is manifested at high temperatures. The determination of the existence of this effect accompanying high-temperature transformations other than martensitic ones and laws of its manifestation is of substantial practice importance, e.g., for the hot deformation of hardly deformable steels [5].

We investigated steel with the composition 1.11 C, 0.16 Si, 0.29 Mn, 1.20 W, 0.72 V, 6.05 Cr, 0.020 P, and 0.018 S (wt %) in the initial state after softening thermal treatment and after rolling at 780°C with a rate of 0.5 m/min (deformation degree ~43%). The temperatures of phase transformations upon heating and cooling were determined by a dilatometer with an inductive sensor [6]. Temperature was measures by a Chromel–Alumel thermocouple whose working seal is in contact with a specimen. The heating rate in the transformation range was equal to about 3°C per minute. Specimens with sizes $2 \times 4 \times 40$ mm were cut from half-finished products in the initial and rolled states. The phase transformations in $2 \times (2.4–4) \times 20$-mm specimens that were heated and cooled under unidirectional compression were studied on the same equipment. Specimens were loaded by means of a press nut whose force was transferred to a specimen through a calibrated spring connected with a quartz pusher. The maximum force was equal to 60 N. Thus, the compressing stress depending on the area of the specimen cross section lied in the range 7.5–12.5 MPa.

High-temperature mechanical tensile tests were carried out on an FP 100/1 testing machine. Two types of specimens were used: first, a cylinder that had 3.0-mm-diameter working sections that had a settlement length of 30.0 mm and were cut from half-finished products in the initial annealed state and, second, 2.0×5.0-mm-section plates that had a settlement length of 20 mm and were cut from half-finished products rolled at 780°C. The temperature of specimens was measured by the Chromel–Alumel thermocouple. The deformation rate was equal to 2 mm/min, corresponding to a strain rate of about 1.1×10^{-3} and 1.7×10^{-3} s^{-1} for cylindrical and planar specimens, respectively.

According to the dilatometric analysis (one of its results is shown by curve *1* in Fig. 1), the $\alpha \longrightarrow \gamma$ phase transformation occurs in the range from 815 (Ac_1) to 863°C (Ac_3) and is accompanied by the contraction of the specimen. It is worth noting that the start temperature of the transformation of the steel under investigation upon heating is much higher (by about 100°C) than the temperature Ac_1 typical for construction steels [7]. The temperature range and mechanism of the $\gamma \longrightarrow \alpha$ transformation upon cooling depend on the temperature variation rate. Upon slow cooling with a furnace, the transformation occurs through the perlite mechanism in

Kurdyumov Institute of Metal Physics and Functional Materials,
Bardin Central Research Institute of Ferrous Metallurgy, Vtoraya Baumanskaya ul. 9/23, Moscow, 107005 Russia
** e-mail: mogutnov@imph.msk.ru*

1028-3358/04/4907-0422$26.00 © 2004 MAIK “Nauka/Interperiodica”

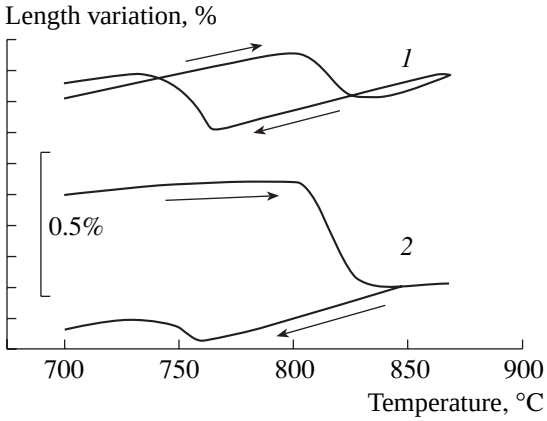

Fig. 1. Dilatograms of a phase transformation in the steel under investigation under heating and slow cooling (*1*) without load and (*2*) with a unidirectional compressing stress of 11.5 MPa.

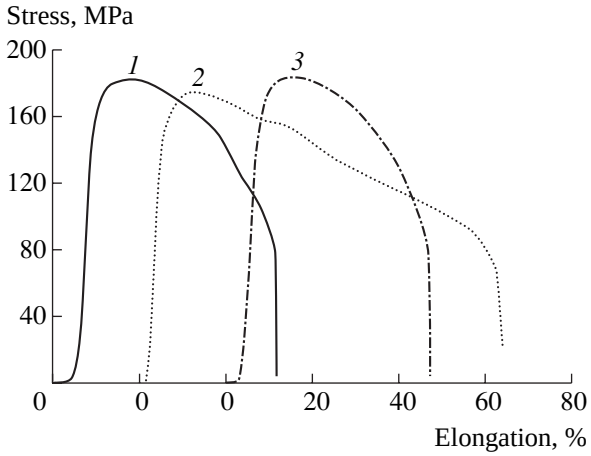

Fig. 2. Tension curves of the steel under investigation in the austenite–carbide state at a temperature of (*1*) 790, (*2*) 800, and (*3*) 810°C.

the temperature range from 780 to 700°C. The temperature range of this transformation depends on the temperature of the metal before cooling, which is associated with the dissolution of carbides and an increase in the stability of austenite due to an increase in the concentrations of carbon and alloying elements in it.

The conditions of high-temperature mechanical tests were chosen by taking into account the determined temperatures of phase transformations. Specimens with the ferrite–carbide structure were studied below 800°C. To obtain the austenite–carbide structure, specimens were heated up to 890°C and then cooled to the test temperature, which was below the start temperature of the $\gamma \longrightarrow \alpha$ transformation. Figure 2 shows the tension curves for specimens with austenite–carbide structures for various temperatures. It is seen that tension curves *1* and particularly *2* are wavy near the transformation temperatures likely due to the development of the transformation in the deformation process. Mechanical tests of specimens made from initial half-finished products (Fig. 3) show that, with an increase in temperature from 700 to 800°C, the strength properties (yield stress and temporal resistance) of steel in the ferrite–carbide state decrease strongly (are almost halved), whereas the relative elongation increases slightly. After the transformation from the ferrite–carbide structure to the austenite–carbide one, the strength increases sharply (is almost doubled) and plasticity decreases. The nonmonotonic temperature dependence of the mechanical properties of the steel under investigation in the austenite–carbide state is the most interesting result. For a temperature of 800°C, which is slightly higher than the start temperature of the $\gamma \longrightarrow \alpha$ transformation upon cooling, curves $\sigma^{\gamma}_{0,2} = f(T)$ and $\sigma^{\gamma}_{B} = f(T)$ have minima (Fig. 3a), the curve $\delta^{\gamma} = f(T)$ has a maximum (Fig. 3b), and the maximum value δ^{γ} is almost twice as large as the relative elongation for lower and higher temperatures. A similar plasticity peak near the start temperature of the transformation upon cooling is also observed in high-temperature tests of specimens made of rolled half-finished products (Fig. 3b).

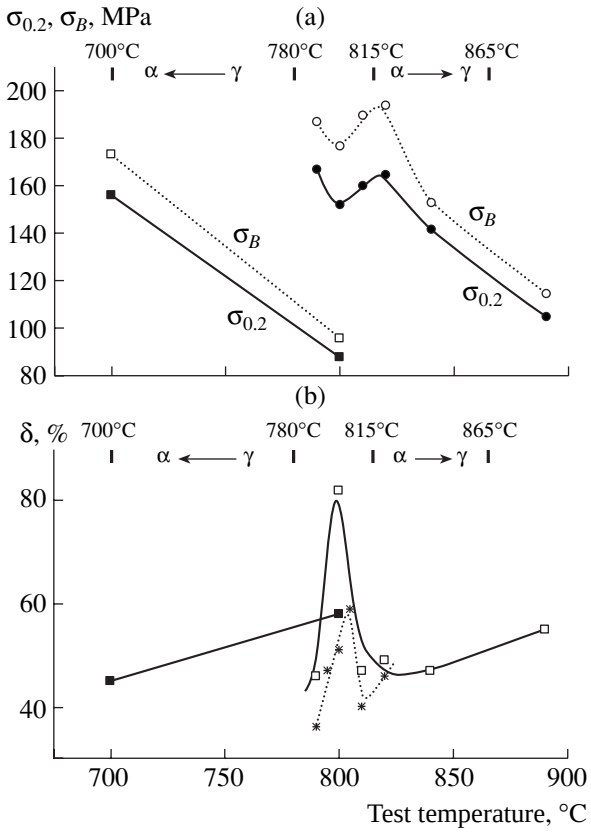

Fig. 3. Temperature dependence of (a) yield stress and temporal resistance for the (squares) ferrite–carbide structure (annealed-steel specimens) and (circles) austenite–carbide structure (annealed-steel specimens); (b) relative elongation for (closed squares) ferrite–carbide structure (annealed-steel specimens), (open squares) austenite–carbide structure (annealed-steel specimens), and (asterisks) austenite–carbide structure (hot-rolled-steel specimens).

Dilatograms of phase transformations under unidirectional compression, which are exemplified by curve *2* in Fig. 1, differ considerably from those obtained in the absence of stresses (curve *1* in Fig. 1), although compressing stresses in experiments were equal to only ~7–10% of the yield stress of steel at transformation temperatures (Fig. 3). Under load, the specimen-length change Δl in the $\alpha \longrightarrow \gamma$ transformation is much larger than that in the $\gamma \longrightarrow \alpha$ transformation. Thus, after the $\alpha \longrightarrow \gamma \longrightarrow \alpha$ transformation cycle under stress, residual strain is comparable with the dilatation effect in the transformation. In the absence of compressing stresses, Δl in the $\alpha \longrightarrow \gamma$ transformation coincides with the value in the $\gamma \longrightarrow \alpha$ transformation, and the residual change of the specimen length after the $\alpha \longrightarrow \gamma \longrightarrow \alpha$ transformation cycle is not observed.

Two features of the mechanical properties of the steel under investigation in the temperature range of phase transformations are worth noting. First, steel in the austenite–carbide state has higher strength and lower plasticity than in the ferrite–carbide state. Second, the properties of steel with the austenite–carbide structure depends nonmonotonically on temperature. The first feature is likely caused by a decrease in volume during the $\alpha \longrightarrow \gamma$ transformation. Due to this decrease, interatomic distances decrease, chemical bonds increase, and strength increases [8, 9]. Nonmonotonic variation of the properties of steel with the austenite–carbide structure is similar to that in the trip effect [4]. The latter effect is an increase in plasticity due to local phase transformations that are stimulated by deformations, give rise to the relaxation of deformation-induced stress peaks, and, therefore, prevent fracture [10]. The trip effect is usually observed during the martensitic transformation. This effect is possibly involved in the formation of the properties of the austenite–carbide state of steel subjected to tensile tests, because relative elongation increases sharply near the start temperature of the $\gamma \longrightarrow \alpha$ transformation, but such a sharp increase is absent at the start temperature of the $\alpha \longrightarrow \gamma$ transformation in the case of the tension of steel with the ferrite–carbide structure (Fig. 3). Indeed, the $\gamma \longrightarrow \alpha$ transformation is associated with an increase in volume, and the elongation of a specimen under tension promotes the development of this transformation, which leads to higher plasticity. On the contrary, extension accompanying the $\alpha \longrightarrow \gamma$ transformation impedes the transformation, and plasticity does not increase. An increase in plasticity in the $\alpha \longrightarrow \gamma$ transformation must be observed under compression. This is corroborated by the results of dilatometric analysis of the transformation under unidirectional compression. According to these results, even small external compressing load (about 1/15–1/10 of the yield stress at the corresponding temperatures) enhances the dilatometric effect that is manifested in the $\alpha \longrightarrow \gamma$ transformation and is associated with a decrease in the volume and length of a specimen. At the same time, this load reduces the dilatometric effect that is manifested in the $\gamma \longrightarrow \alpha$ transformation and is associated with an increase in volume (curve *2* in Fig. 1). The narrowness of the temperature range of anomalously high plasticity is also consistent with the trip effect, which is observed in a narrow temperature range near the start temperature of the transformation [4].

The above sharp increase in the relative elongation can be caused by structural superplasticity, in the presence of which large uniform deformation of metal is not accompanied by strain hardening. Structural superplasticity is observed for temperatures above $0.4T_{melt}$, a grain size in the range 3–5 μm, and a strain rate in the range 10^{-4}–10^{-3} s^{-1} [3]. We carried out mechanical tests at 700–900°C with a rate of about 10^{-3} s^{-1} and with the size of the ferrite grain in the range 1–5 μm. Thus, all conditions for the manifestation of superplasticity were satisfied in tests, and structural superplasticity would contribute to the general plasticity. However, high plasticity is observed only in a narrow temperature range near the start temperature of the $\gamma \longrightarrow \alpha$ transformation, and the tension curves are wavy (Fig. 2). These circumstances indicate that high plasticity is attributed to the phase transformation, and the contribution of structural superplasticity is hardly significant.

Steel in the ferrite-carbide state in the temperature range near the start temperature of the transformation under heating is characterized by the combination of strength and plasticity. According to the temperature dependence of these properties, this combination in the austenite–carbide structure is reached at temperatures 150–200°C higher. This combination of the properties allows the hot deformation of steel in the α region at lower temperatures near the start temperature of the transformation under heating. Such a treatment can be energy profitable, prevent the growth of grains, and reduce the oxidation and loss of carbon. However, the temperature range for this treatment is rather narrow, because a decrease in temperature rapidly reduces plasticity and increases strength, which is attributed to the strong temperature dependence of the mechanical properties, and an increase in temperature sharply increases strength and reduces plasticity, which is attributed to the appearance of austenite. The above technological possibility arises due to a high temperature Ac_1 of about 815°C, which is about 100°C higher than the corresponding temperature in usual non-alloy and low-alloy steels. This feature of the steel being investigated is associated with a high content of strong carbide-forming elements that provide a low carbon content in ferrite in equilibrium with carbides. Therefore, the high temperature Ac_1 of the transformation and, correspondingly, the above technological possibilities must be inherent in many tool steels, as well as low-carbon car-sheet and low-silicon electrical steels.

ACKNOWLEDGMENTS

This work was supported by the OAO MMK Foundation, Ausferr Engineering Center, and Intels Foundation for Science and Education (project no. 07-03-02).

REFERENCES

1. R. H. Johnson and G. W. Greenwood, in *Proceedings of the Conference on the Relations between the Structure and the Mechanical Properties of Metals* (London, 1968).
2. E. I. Estrin, J. Phys. IV **6** (C1), 429 (1996).
3. M. Kh. Shorshorov, A. S. Tikhonov, S. I. Bulat, *et al.*, *Superplasticity of Metallic Materials* (Nauka, Moscow, 1973).
4. I. Ya. Georgieva, Itogi Nauki Tekh., Ser.: Metalloved. Term. Obrab. **16**, 69 (1982).
5. A. P. Gulyaev, *Superplasticity of Steel* (Metallurgiya, Moscow, 1982).
6. É. I. Éstrin, Zavod. Lab., No. 3, 368 (1966).
7. V. G. Sorokin, A. V. Volosnikova, S. A. Vyatkin, *et al.*, *Grades of Steels and Alloys: A Handbook* (Mashinostroenie, Moscow, 1989).
8. É. Gudremon, *Special Steels* (Metallurgizdat, Moscow, 1959), Vol. 1, p. 78.
9. M. L. Cohen, Phys. Rev. B **32**, 7988 (1985).
10. Yu. G. Virakhovskiĭ, I. Ya. Georgieva, Ya. B. Gurevich, *et al.*, Fiz. Met. Metalloved. **32**, 348 (1971).

Translated by R. Tyapaev

Doklady Physics, Vol. 49, No. 7, 2004, pp. 426–427. Translated from Doklady Akademii Nauk, Vol. 397, No. 3, 2004, pp. 334–336.

ENERGETICS

Free Convective Heat Transfer in a Square Cavity with Periodic Temperature Variation on One of the Walls

P. T. Zubkov, M. V. Kanashina, and E. V. Kalabin

Presented by Academician A.I. Leont'ev December 30, 2003

Received March 15, 2004

INTRODUCTION

Unsteady free convective heat transfer in cavities with periodic temperature variation on one of their walls was rather thoroughly studied in the last two decades. In particular, a square cell with isothermal vertical and adiabatic horizontal walls was analyzed in [1, 2] (in the latter paper, works on the problem under consideration were also reviewed). Such problems are of interest due to their importance for understanding various phenomena arising in a number of technological processes (e.g., cooling electric circuits, use of solar energy, heating and cooling rooms, etc.).

Almost all previous works were devoted to systems where the temperatures of opposite walls were initially different and the temperature of the hot wall varied such that the average temperature was equal to its initial temperature. However, the temperature of the cold wall varied (i.e., its average temperature was lower than the temperature of the opposite wall) in the case considered in [3]. It was found that, for a certain range of parameters and a rather large amplitude of temperature oscillations, the total heat flux can be directed from the cold wall to the hot one.

In this work, we consider boundary conditions such that the time-averaged temperatures of opposite walls of an inclined square cell are identical. It is shown that the total heat flux through the cavity is absent and present when the walls are vertical isothermal and inclined at a certain angle, respectively. For practice, it is important to increase the time-averaged heat flux through the cell (particularly in view of the absence of the heat flux through the cell under stationary boundary conditions). For this reason, particular attention is paid to the dependence of the total heat transfer at various Grashof numbers on both the temperature oscillation frequency and the inclination angle of the cavity.

Tyumen State University,
ul. Semakova 10, Tyumen, 625003 Russia
e-mail: pzubkov@utmn.ru

SETTING OF THE PROBLEM

We numerically study unsteady free convection in an inclined square cavity. Two opposite walls horizontal at the zero inclination angle are thermally isolated. At the right boundary, constant temperature T_0 is given, whereas the temperature of the left boundary varies as $T(t) = T_0 + \Delta T \sin \omega t$. We assume that the flow is two-dimensional and laminar, the fluid is incompressible, and all its temperature properties are constant (except the density in the source term in the equation of motion).

Since we analyze a periodic process arising long after the initial instant, we deal with a class of problems having no initial conditions. Thus, the solution is also independent of them. Passing to a dimensionless system of equations (see [3] for details), we arrive at the following dimensionless parameters: the Grashof number $\mathrm{Gr} = \dfrac{g\beta\Delta T L^3}{\nu^2}$, the Prandtl number $\mathrm{Pr} = \dfrac{\mu c}{\lambda}$, and the dimensionless frequency $f = \dfrac{\omega \rho_0 L^2}{\mu}$. In the given case, the dimensionless amplitude of temperature variations at the boundary is equal to unity.

The cavity is filled with air, for which Pr = 1. The results are obtained for inclination angles $0° \le \alpha \le 90°$ and two Grashof numbers $\mathrm{Gr} = 2 \times 10^5$ and 3×10^5. All calculations were performed by the control volume method with the SIMPLER algorithm [4] on a 52×52 mesh. The time step was equal to 4×10^{-6}. Thus, for $f = 20\pi$, it took us 25000 time steps to pass one period.

RESULTS OF CALCULATIONS

For $\alpha = 0°$, the heat flux through the cavity varies with time almost as a sinusoid. However, with increasing inclination angle, the behavior of the heat flux changes and becomes more complicated. With an increase in the temperature oscillation frequency at the boundary, the amplitude of the heat flux variation on the right wall decreases (a similar behavior is also observed for pure heat conduction without convection). With

1028-3358/04/4907-0426$26.00

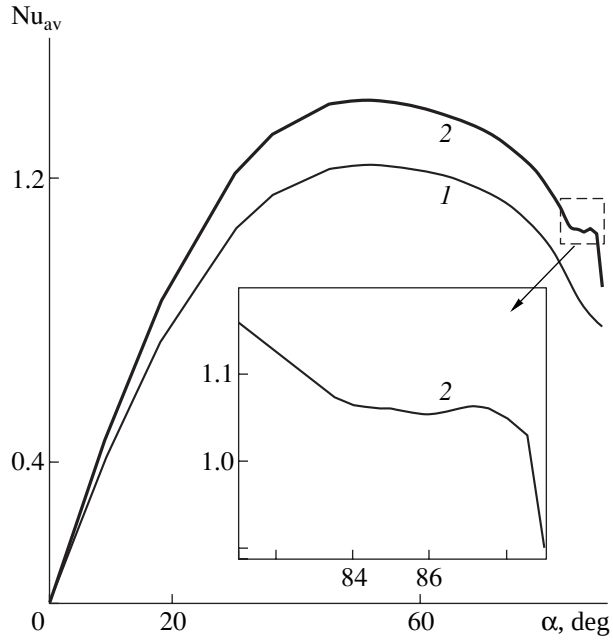

Fig. 1. Time-averaged heat flux Nu_{av} as a function of the cavity inclination angle α at a temperature oscillation frequency of $f = 20\pi$ for Grashof numbers (*1*) $Gr = 2 \times 10^5$ and (*2*) 3×10^5.

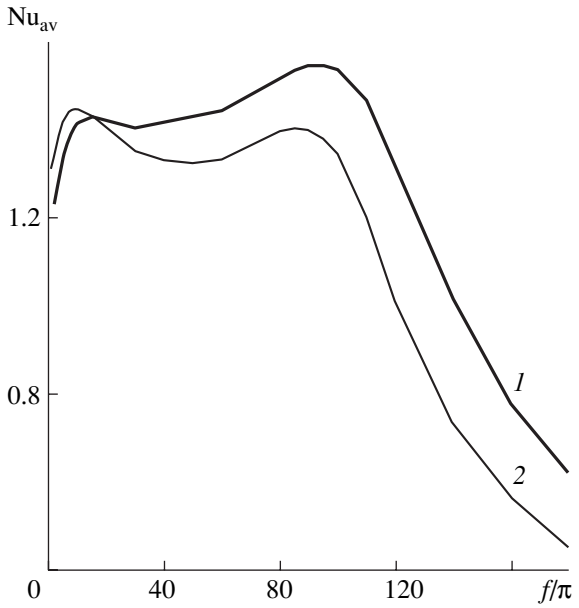

Fig. 2. Time-averaged heat flux Nu_{av} as a function of the temperature oscillation frequency f for Grashof number $Gr = 3 \times 10^5$ at cell inclination angles of (*1*) 50° and (*2*) 60°.

increasing frequency, the total heat flux through the cell also decreases and vanishes in the limiting case $f \longrightarrow \infty$.

Analysis of the fields of both the stream function and temperature shows that the flow pattern varies very strongly during the oscillation period. One, two, and three vortices having different rotation directions are observed within the cavity at certain times.

We now consider the time-averaged heat flux Nu_{av} across the cell as a function of the inclination angle at a fixed frequency $f = 20\pi$ (Fig. 1). As was expected, at $\alpha = 0°$, the zero heat flux is transferred through the cell in the oscillation period, whereas at $\alpha \neq 0°$, heat is transferred from the left wall to the right one. The transfer is maximal at $\alpha = 54°$ (for both Grashof numbers). In addition, for $Gr = 3 \times 10^5$, a local minimum and maximum of the heat transfer are observed near $\alpha = 90°$, which is associated with a significant rearrangement of the flow near this inclination angle.

The variation of the total heat flux across the cavity as a function of the frequency f at $\alpha = 50°$ and 60° is presented in Fig. 2 for $Gr = 3 \times 10^5$. These dependences are significantly nonlinear. For example, for $\alpha = 60°$, a local minimum at $f = 50\pi$ and two maxima at $f = 10\pi$ and 85π are observed. The variation of the heat flux intensity in the frequency range from 5π to 100π does not exceed 10%. A further increase in the frequency ($>100\pi$) is accompanied by a rapid decrease in the heat transfer through the cavity.

CONCLUSIONS

Thus, the free-convective heat transfer in an inclined square cavity with a periodic temperature variation on one of the walls was numerically analyzed. It is important that the time-averaged temperature of this wall coincided with the constant temperature of the opposite wall.

It was shown that, at inclination angles $\alpha \neq 0°$, the heat flux averaged over the oscillation period is directed to the constant-temperature wall. The total heat flux was found as a function of the temperature oscillation frequency at fixed cell inclination angles for $Gr = 2 \times 10^5$ and 3×10^5. The dependence of the heat flux intensity on the inclination angle was analyzed for various oscillation frequencies. It was shown that, for these Grashof numbers, the maximum heat transfer through the cavity is reached for an angle inclination of $\alpha = 54°$ and temperature oscillation frequency of $f = 20\pi$.

REFERENCES

1. M. Kazmierczak and Z. Chinoda, Int. J. Heat Mass Transf. **35**, 1507 (1992).
2. H. S. Kwak, K. Kuwahara, and J. M. Hyun, Int. J. Heat Mass Transf. **41**, 2837 (1998).
3. P. T. Zubkov, M. V. Kanashina, and E. V. Kalabin, Teplofiz. Vys. Temp. **42**, 118 (2004).
4. S. Patankar, *Numeral Heat Transfer and Fluid Flow* (McGraw-Hill, New York, 1980; Énergoatomizdat, Moscow, 1984).

Translated by G. Merzon

Doklady Physics, Vol. 49, No. 7, 2004, pp. 428–430. Translated from Doklady Akademii Nauk, Vol. 397, No. 1, 2004, pp. 49–51.

MECHANICS

Transitions between Regimes of a Flow around Two Tandem-Arranged Plates

A. V. Gudzovskiĭ

Presented by Academician O.M. Belotserkovskiĭ March 4, 2004

Received March 10, 2004

Types of the phase diagram of a plane flow near two tandem-arranged bluff bodies are analyzed. It is known that plane flows near two commensurate bluff bodies separated by a distance G are characterized by a common property: there is a critical gap G' such that the frequency of vortex shedding f for $G < G'$ strongly differs (by 10–50%) from that for $G > G'$.

The jump change in f upon varying G is observed in a wide range of Reynolds numbers Re for bodies of various shapes such as a pair of circular cylinders [1], a circular cylinder, and a splitter plate that is placed behind the cylinder and oriented along the free flow [2–4], and transverse plate (cylinder with the rectangular cross section with a side ratio of 10 : 1) with a splitter behind it [3].

The effect is attributed to the difference between the flow structures in the U (unified) regime for $G < G'$ and in the D (double) regime for $G > G'$. In the U regime, a pair of bodies is streamlined almost as a whole and the vortex street consists of vortices formed behind both bodies. In the D regime, vortices are formed on the first body lying upstream such that the second body is inside the vortex street.

The dimensionless variables are obtained by dividing by the length d (cylinder diameter or plate width), velocity V of the free flow, and time $\frac{d}{V}$. The Reynolds number is equal to $\mathrm{Re} = \frac{Vd}{\nu}$, where ν is the kinematic viscosity.

1. A jump (hard) transition between the flow regimes with different structures must be accompanied by hysteresis, which was not observed in many experiments [1–4] but was observed, e.g., in [5]. It is reasonable to assume that the hard transition between the U and D regimes with hysteresis occurs in a flow near a pair of commensurate bluff bodies of arbitrary shapes for $\mathrm{Re} > 100$. On the (Re, G) plane, the interfaces between regimes lie in the band $G_1 < G < G_2$, where $G_1 \approx 1$ and $G_2 \approx 6$ [1–5].

For low Re values, the steady S regime of the flow near a pair of bluff bodies loses stability. On the (Re, G) plane, the boundary of the S-regime stability lies in the band $\mathrm{Re}_1 < \mathrm{Re} < \mathrm{Re}_2$, where $\mathrm{Re}_1 \approx 20$ and $\mathrm{Re}_2 \approx 70$. The transition through this boundary is continuous (soft).

If each regime is treated as an individual phase, the following two types of the phase diagram are possible on the (Re, G) plane.

(i) A diagram where the stability boundaries of the U and D regimes are united to the unified boundary at the triple point (Re_3, G_3) upon decreasing Re. This unified boundary further passes until the intersection with the stability boundary of the S regime (the transition between the U and D regimes is hard with hysteresis and soft reversible for $\mathrm{Re} > \mathrm{Re}_3$ and $\mathrm{Re} < \mathrm{Re}_3$, respectively).

(ii) A diagram that has no triple point and in which the transition between the U and D regimes is hard for all Re values (stability boundaries of the U and D regimes intersect the stability boundary of the S regime at different points).

In this work, both types of phase diagram for $\mathrm{Re} < 100$ are obtained for a flow around a pair of plates with different orientation of the downstream plate.

2. Let us consider a plane flow of an incompressible fluid around two identical plates with length $L \gg 1$ and thickness $\delta \ll 1$. The free flow is directed along the x axis, and the coordinate origin is at the center of the first plate P_1 oriented across the flow (along the y axis). We consider two orientations of the second plate placed downstream at distance G from the first plate. The first orientation is along the flow (P_1S configuration with the plate P_1 and splitter plate S in the near wake), and the second configuration is across the flow (P_1P_2 configuration of a tandem of the plates P_1 and P_2). The splitter plate in the P_1S configuration suppresses the transverse velocity component v in the wake, and the second plate in the P_1P_2 configuration suppresses the longitudinal velocity component u.

Institute of Design Automation,
Russian Academy of Sciences, Moscow, 123056 Russia
e-mail: agudzovsky@mtu-net.ru

1028-3358/04/4907-0428$26.00 © 2004 MAIK “Nauka/Interperiodica”

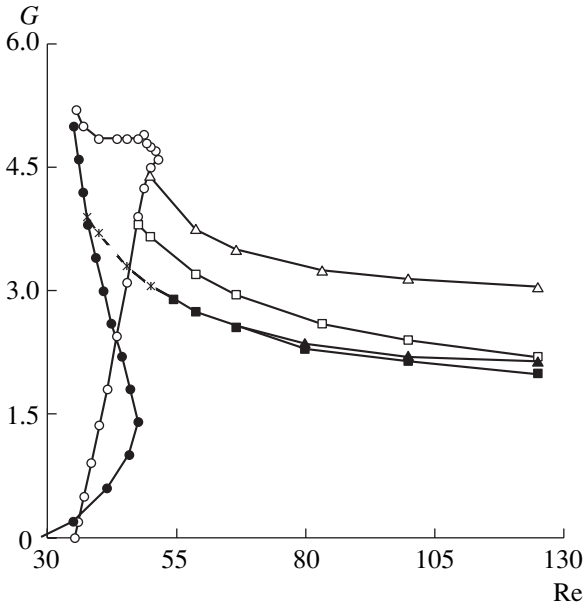

Fig. 1. Stability boundaries for (circles) S, (triangles and asterisks) U, and (squares and asterisks) D regimes for the (open symbols) P_1S and (closed symbols and asterisks) P_1P_2 configurations. The boundary of the soft reversible transition between the U and D regimes in the P_1P_2 configuration is shown by the asterisks and dashed line.

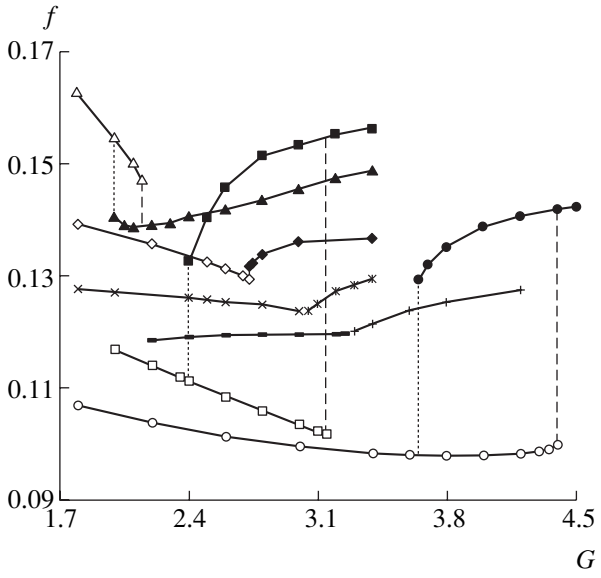

Fig. 2. Frequencies (open symbols, ×, –) $f(G_U)$ and (closed symbols, ⁎, +) $f(G_D)$ for Re = (circles) 50 and (squares) 100 in the P_1S configuration and for Re = (–, +) 45.5, (×, ⁎) 50, (diamonds) 58.8, and (triangles) 125 in the P_1P_2 configuration. The dashed and dotted lines show the transitions at G'_U and G'_D, respectively.

Numerical experiments were carried out by the Flow Vision code [6]. The velocity and pressure fields were determined by integrating the Navier–Stokes equations on a staggered Cartesian grid by an explicit finite-volume method such as the projection method. The usual boundary conditions are specified both on the boundaries of the rectangular computational domain given by the inequalities $-10 \le x \le 60$ and $|y| \le 15.5$ and on the plates [7]. The steps of the computational grid increase from $\Delta x = \Delta y = 0.05$ near the plates and in the near wake ($(|y|) \le 1.5$, $-0.2 \le x \le 7$) to $\Delta x = \Delta y = 0.5$ on the periphery.

3. The stability boundary of the S regime on the (Re, G) plane is determined by the method described in [7]. A stationary solution of the Navier–Stokes equations that is symmetric about the x axis is preliminarily found for a pair of Re and G. Small symmetry-breaking perturbation is introduced to the solution by a short-term increase in the width of the first plate by 0.05. Perturbation either is damped and the flow returns to the initial steady state or is developed to an oscillatory flow.

Figure 1 shows the stability boundaries for the S regime near both configurations. The splitter stabilizes the flow near P_1S until it is located within the domain with a pair of bound vortices. For $G > 4.85$, the flow is transformed to the D regime.

4. The stability boundaries G'_U (Re) and G'_D (Re) for the U and D oscillatory regimes, respectively, are found for $40 \le \mathrm{Re} \le 125$ (Fig. 1). For each Re value, sequences of steady flows in the U and D regimes are obtained for a number of gap values G_U and G_D, respectively. The initial approximation for computation of these flows is taken in the form of a flow in the same regime but for other G or Re values. This approach simulates the formation of a new flow in a physical experiment by quasi-stationary variation of G or V.

When the gap G_U exceeds its upper limit G'_U, the U regime is transformed to the D regime. When the gap G_D becomes lower than its lower limit G'_D, the D regime is transformed to the U regime.

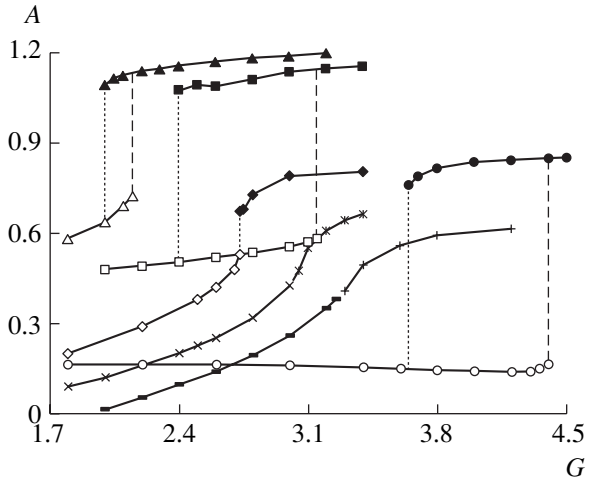

Fig. 3. Same as in Fig. 3 but for the amplitudes $A(G_U)$ and $A(G_D)$.

Figure 2 and 3 show the G dependences of the frequency f and amplitude A, respectively, of steady-state oscillations for both configurations with certain Re values. The amplitude A is determined as the maximum of the transverse velocity component $v(x, y, t)$ in the segment of the x axis between the plates; i.e., $A = \max_{0 \le x \le G} v(x, 0, t)$, where t is the time within the oscillation period. The phase diagrams of flows near P_1P_2 and P_1S refer to the first (with the triple point) and second types, respectively.

The hard transition for both configurations is manifested as a discontinuity of the functions $f(G)$ and $A(G)$. On the boundary of the soft (continuous) transition between the U and D regimes for the flow near P_1P_2, the first derivative of the function $f(G)$ or the second derivative of the function $A(G)$ is discontinuous. We emphasize that these flow regimes are virtually indistinguishable in the soft-transition domain. Therefore, the transition boundary can be found only indirectly as a singular point of the function $f(G)$ or $A(G)$.

The triple point $\mathrm{Re}_3 = 54.5$ for P_1P_2 is found from the Re dependence of the amplitude jump $\Delta A = A_D - A_U \sim (\mathrm{Re} - \mathrm{Re}_3)^{1/2}$ in the hard transition.

A regime near the hysteresis domain $G'_D < G < G'_U$ is determined by the initial conditions. The U regime is realized in this G range when the initial conditions correspond to a U-regime flow or rest state. This conclusion explains the absence of hysteresis in experiments reported in [1–3], where G was likely varied with a turned-off aerodynamic tube. In [4], the results were obtained by a continuous increase in G, and the transformation of the flow upon decreasing G was not analyzed. In other words, the absence of hysteresis in [1–4] is explained by the procedure of the formation of the flow for $G'_D < G < G'_U$.

ACKNOWLEDGMENTS

I am grateful to É.G. Shifrin for attention to the work.

REFERENCES

1. M. M. Zdravkovich, ASME Trans. J. Fluids Eng. **99**, 618 (1977).
2. A. Roshko, J. Aeronaut. Sci. **22**, 124 (1955).
3. S. Ozono, Phys. Fluids **11**, 2928 (1999).
4. J.-Y. Hwang, K.-S. Yang, and S.-H. Sun, Phys. Fluids **15**, 2433 (2003).
5. T. Igarashi, Trans. Jpn. Soc. Mech. Eng., Ser. B **46**, 1026 (1980).
6. A. V. Gudzovskiĭ, Zh. Vychisl. Mat. Mat. Fiz. **41**, 1250 (2001).
7. A. V. Gudzovskiĭ, Izv. Ross. Akad. Nauk, Mekh. Zhidk. Gaza, No. 2, 56 (2003).

Translated by R. Tyapaev

Doklady Physics, Vol. 49, No. 7, 2004, pp. 431–435. Translated from Doklady Akademii Nauk, Vol. 397, No. 1, 2004, pp. 52–56.

MECHANICS

Integral-Approach Simulation of the Kinetics of the Formation of Particles in Disperse Systems

V. N. Piskunov

Presented by Academician R.I. Il'kaev February 17, 2004

Received February 26, 2004

In many applied problems of the physics of disperse systems, it is sufficient to know the integral characteristics of the particle spectrum n without detailed information on the distribution function $n(g, t)$ over masses g. An approach simulating the behavior of a disperse system by using integral quantities must provide a considerable gain in the calculation speed. Simulation of the coagulation process is most laborious. A closed formulation of the problem that allows the description of the kinetics of coagulation in terms of integral quantities was given in [1, 2], and the genetic algorithm (GA) method developed for its solution was described in detail in [3].

However, coagulation, together with other processes, cannot be calculated only with integral quantities. In particular, loss of particles due to their complete evaporation is determined by the flux $n(0)v(0)$, where $v(g)$ is the condensation rate, and calculation of spatial diffusion by the sweep method requires the transfer of n values onto the given common grid $\{G_k\}$, etc. The joint simulation of coagulation and condensation is most important for practical applications.

1. The kinetic equation jointly describing coagulation and condensation has the form

$$\partial_t n(g, t) + \partial_g[v(g)n(g)] = \frac{1}{2}\int_0^g K(g-s, s) \times n(g-s)n(s)ds - n(g)\int_0^\infty K(g, s)n(s)ds. \quad (1)$$

Here, t is time, $n(g, t)$ is the density (spectrum) of particles with mass g, $v(g)$ is the rate of the condensation growth (evaporation) of particles, and $K(g, s)$ is the coagulation coefficients. To solve Eq. (1), we use the method of decomposing into physical processes [4]. According to this method, two equations,

$$\partial_t n(g, t) = \frac{1}{2}\int_0^g K(g-s, s)n(g-s)n(s)ds - n(g)\int_0^\infty K(g, s)n(s)\,ds, \quad (1a)$$

$$\partial_t n(g, t) + \partial_g[v(g)n(g)] = 0 \quad (1b)$$

are simultaneously solved at each time step Δt. The coagulation kinetic equation in integral form (1a) is solved by the GA method, where the generalized approximation of the spectrum on a grid with variable nodes $g_i(t)$, $1 \le i \le I$ is used. In [2, 3], an algorithm for constructing a dynamic grid $\{g_i(t)\}$ was described, and it was shown that the use of variable nodes reduces the laboriousness of calculations and increases the calculation accuracy. Condensation kinetic equation (1b) is solved by the particle method (see, e.g., [5]). In both methods, spectra are approximated by sets of delta functions with variable particle masses:

$$n(g, t) = \sum_{i=1}^{I} n_i(t)\delta[g - g_i(t)]. \quad (2)$$

Strictly speaking, Eq. (2) is the generalized approximation of solutions and can be used only for the description of the integral parameters of the spectrum. In particular, approximation (2) makes it possible to determine the integral moments

$$L_m(t) \equiv \int_0^\infty g^m n(g, t)\,dg = \sum_{i=1}^{I} n_i(t)g_i^m \quad (3)$$

of the function $n(g, t)$. As a basis set, we actually use the functions $\varphi_p(g) = g^{(p-1)/6}$, $p = 1, 2, \ldots, 2I$; i.e., the parameter m takes the values $0, \frac{1}{6}, \ldots, \frac{2I-1}{6}$. The GA

Russian Federal Nuclear Center VNIIÉF, pr. Mira 37, Sarov, Nizhegorodskaya oblast, 607188 Russia
e-mail: piskunov@vniief.ru

1028-3358/04/4907-0431$26.00 © 2004 MAIK "Nauka/Interperiodica"

method ensures a high accuracy of the description of dynamic parameters already for a small number $I = 4$ [6]. However, the correct description of condensation kinetics requires a larger number $I \geq 10$–20 of variable points. The reason is that points falling within the domain $g_p \leq 0$ (complete evaporation of particles) must be excluded from the calculation; i.e., calculations of condensation kinetics require storage of points that must be continuously supplemented.

2. Thus, the transition from calculation of the kinetics of coagulation to simulation of condensation requires a procedure of increasing the number I of grid nodes and determining the densities (spectra) of particles at them. In calculations for particular systems [7], there is an attempt to solve this problem by approximating the spectra by various functional dependences and then calculating necessary values at any nodes. Results obtained in [7] and our calculations with the reconstruction of the spectra of particles in terms of moments L_m show that no available approximation universally reconstructs all typical spectra with satisfactory accuracy. The basic difficulty is that any specific approximation determines the explicit behavior or singularity for the spectrum for $g \gg 1$ and $g \longrightarrow 0$, while these characteristics are known neither theoretically nor numerically.

In view of this circumstance, let us describe an algorithm that provides an increase in the number I of grid nodes and determination of the particle spectra at them, holding the exact values of the moments L_m. In this algorithm, generalized approximation (2) is associated with piecewise continuous spectra determined on the finite segment $\Delta = [0, g_{\max}]$. In this approach, it is not necessary to know the behavior of the spectra for $g \gg 1$ and $g \longrightarrow 0$. This substantially simplifies the problem: only discrete values $\tilde{n}_i$ in a finite number of segments $\Delta_i = [\tilde{g}_{i-1}, \tilde{g}_i]$, $i = 1, 2, \ldots, I$, must be determined.

Thus, let us consider the generalized approximation of the spectra $n(g, t)$ in the form of the set of I delta functions (2) with variable particle masses g_i and determine $2I$ integral moments L_m with $m = 0, \frac{1}{6}, \ldots, \frac{2I-1}{6}$ from Eq. (3). The spectrum consisting of I steps is constructed in terms of these $2I$ integral moments L_m. The limit points of the corresponding segments $\Delta_i = [\tilde{g}_{i-1}, \tilde{g}_i]$ and spectral values $\tilde{n}_i$ in them are determined from $2I$ equations

$$\sum_{i=1}^{I} \tilde{L}_m^i = L_m, \quad \tilde{L}_m^i \equiv \int_{\Delta_i} g^m \tilde{n}\, dg = \frac{\tilde{n}_i}{m+1}(\tilde{g}_i^{m+1} - \tilde{g}_{i-1}^{m+1}), \tag{4}$$

$$\tilde{g}_0 = 0, \quad m = 0, \frac{1}{6}, \ldots, \frac{2I-1}{6}.$$

The step approximation yields not only integrals over the entire segment Δ but also quite accurate values of the integrals $\tilde{L}_m^i$ within the segments Δ_i. These values are consistent with the exact integrals over the entire spectrum, because $\sum_{i=1}^{I} \tilde{L}_m^i = L_m$. This interpretation immediately provides the following procedure of multiple reproduction of nodes. First, I segments Δ_i with I piecewise constant spectral values $\tilde{n}_i$ are constructed by Eqs. (4) in terms of $2I$ moments (3) and I delta functions (2). Second, the parameters of I^2 delta functions similar to Eq. (2) are determined in terms of the partial moments $\tilde{L}_m^i$ (their number is equal to $I \times 2I = 2I^2$) calculated in these segments. The new values n_k and g_k are determined from $2I^2$ equations

$$\sum_{k=1}^{I} n_k g_k^m = \tilde{L}_m^i, \quad m = 0, \frac{1}{6}, \ldots, \frac{2I-1}{6}, \tag{5}$$

$$i = 1, 2, \ldots, I.$$

Continuing the procedure, one obtains I^N delta functions at the Nth step. In practice, it is sufficient to use $I = 4$ and $N = 2$. The procedure of the reproduction of nodes is illustrated in Figs. 1 and 2, where the cumulative quantities

$$N_{\text{cum}}(g) = \int_0^g n(g')\, dg', \quad M_{\text{cum}}(g) = \int_0^g n(g') g' dg'$$

are shown for the lognormal distribution and spectrum $n(g) = g\exp(-g)$, respectively. It is seen that the addition of points corresponds well to the dependences for the original continuous spectrum.

3. The integral simulation of the kinetics of coagulation and condensation is numerically realized as follows. The kinetics of coagulation is calculated by the GA code taken from [5] with $I = 4$. Condensation is calculated by the particle method [4] with $I = 4$ and 16. The above algorithm of $4 \longrightarrow 16$ point reproduction is used to pass from the simulation of coagulation to condensation (reverse rearrangement of points is trivial). The resulting software package is called the AerosGA code, and it is tested on two problems.

The first test is performed for analytical solutions of general kinetic equation (1) of coagulation and condensation that are obtained in [5, 8] for model coagulation kernels $K(g, s)$, $K_c = 2$, $K_+ = g + s$, and $K_* = 2gs$, and for monotonic condensation rates $\nu(g, t) = \beta(t)g$. Calculations by the AerosGA code were performed for the kernel K_+ and $\beta = \text{const} = 1$. We emphasize that coagula-

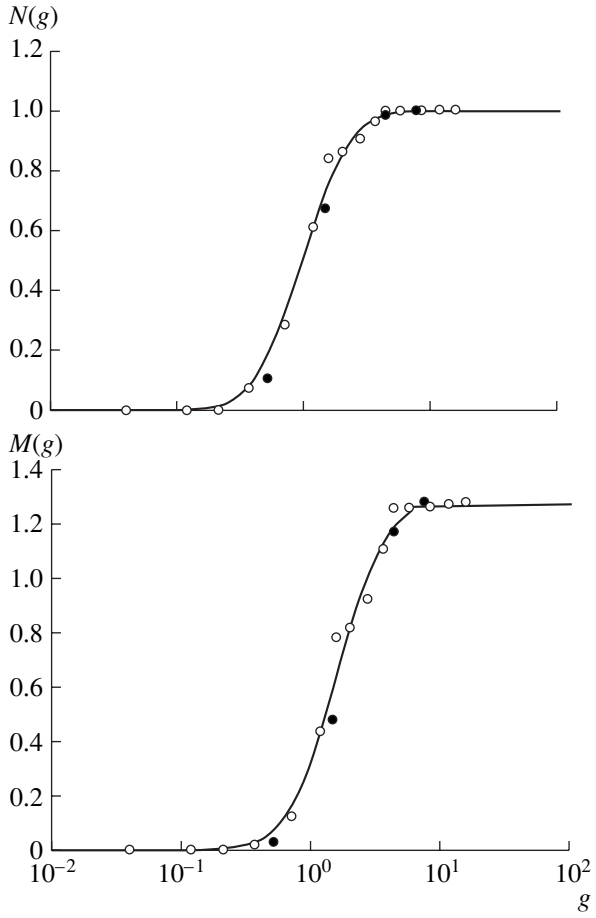

Fig. 1. Approximation for the lognormal spectrum. $I = 4$ (●), 16 (○).

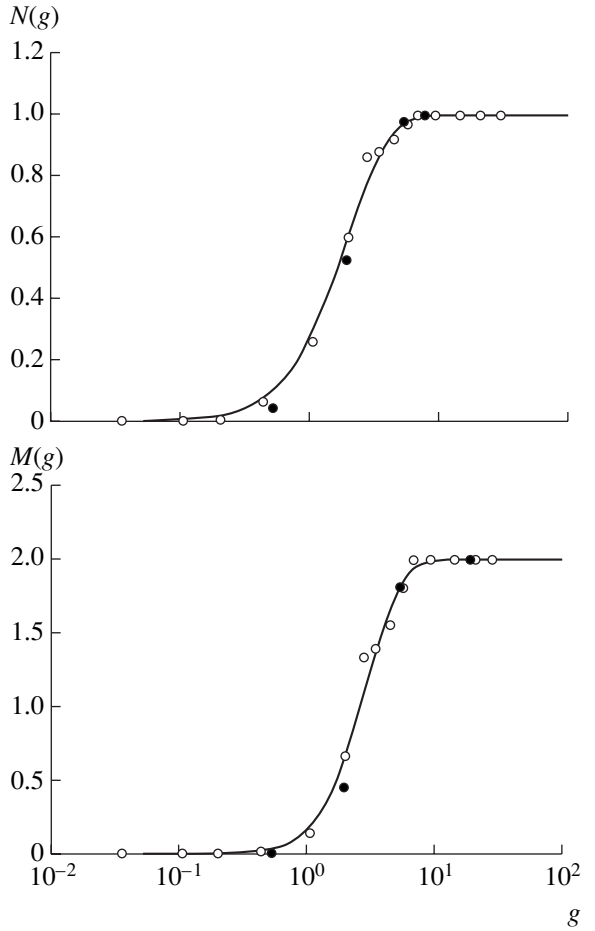

Fig. 2. Approximation for $n(g) = g\exp(-g)$. $I = 4$ (●), 16 (○).

tion with the kernel K_+ leads to strongly polydisperse spectra [5] and the average size changes by six orders of magnitude after dimensionless time $t = 2.5$. Therefore, this test is very critical. Comparison was made for the cumulative quantities

$$N_{\text{cum}}(g, t) = \int_0^g n(g', t)\, dg',$$

$$M_{\text{cum}}(g, t) = \int_0^g n(g', t) g' dg'.$$

Up to time $t = 2.5$, the AerosGA code yields $N(t) = N_{\text{cum}}(\infty, t)$, coinciding with the analytical solution within an accuracy of 3%. Figure 3 illustrates the accuracy of the reproduction of the cumulative quantities for various g values. It is important that calculations by the AerosGA code are free of instabilities or oscillations.

In the second test problem, we note that condensation rates $v(g)$ in real disperse systems are negative for small drop sizes g. Therefore, small drops are completely evaporated and the total computational density $N(t)$ decreases. This feature was used in classical work [9] to describe the asymptotic regimes of the growth of new-phase nuclei in supersaturated solid solutions.

Let us consider a model case where the condensation rate is given by the expression [10]

$$v(g, t) = \chi\left(\frac{g}{g_*(t)} - 1\right), \quad g_*(t) = \frac{1 - M(0)}{1 - M(t)}. \quad (6)$$

Here, χ is a constant, $M(t)$ is the mass density, and $g_*(t)$ is the critical drop size for which the growth rate $v(g)$ changes sign. The densities of vapor and drops are normalized to the final value $M(\infty)$, and mass g is normalized to the initial mass $g_*(0)$ of the critical drop. Dependences (6) seem to be quite realistic, because only change $g_*(t) \longrightarrow g_*^{1/3}(t)$ is necessary for small supersaturations and the diffusion regime of the supply of vapor to drops [5, 9].

An analytical solution of condensation kinetic equation (1b) for model (6) was obtained in [10] disregarding coagulation. Let us solve Eqs. (1) for model (6) and

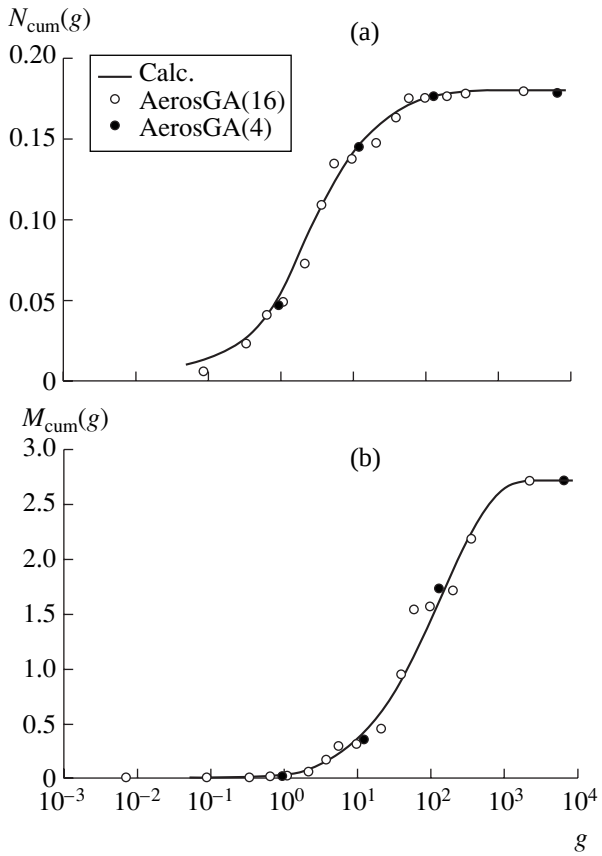

Fig. 3. Cumulative quantities (a) $N_{cum}(g)$ and (b) $M_{cum}(g)$ for $t = 1$.

constant coagulation rates $K(g, s) = K_c = 2Q$. In this case, direct substitution into Eqs. (1) shows that, for the initial spectrum $n_0(g) = a\exp(-gb)$, the solution for all t values has an exponential form similar to [10]:

$$n(g, t) = A(t)\exp[-gB(t)], \tag{7}$$

where

$$A(t) = au(t)\exp\left[-b\chi\int_0^t u(\tau)\,d\tau\right],$$

$$u(t) = \exp\left(-\chi\int_0^t \frac{d\tau}{g_*(\tau)}\right), \quad B(t) = bu(t).$$

Integrating spectrum (7) with respect to g, one obtain the relations

$$N(t) = \frac{A(t)}{B(t)}, \quad M(t) = \frac{A(t)}{B^2(t)}$$

of $A(t)$ and $B(t)$ with the number $N(t)$ and mass $M(t)$ densities. The behavior of $A(t)$ and $B(t)$ is determined by the differential equations

$$d_tB(t) = -\frac{\chi B(t)}{g_*(t)} - QA(t),$$
$$d_tA(t) = -\chi A(t)\left[B(t) + \frac{1}{g_*(t)}\right] - \frac{2QA^2(t)}{B(t)}. \tag{8}$$

Taking into account that $u(0) = 1$, we obtain the initial conditions $A(0) = a$ and $B(0) = b$. According to Eq. (6), the quantities $A(t)$ and $B(t)$ are related to $g_*(t)$ as

$$g_*(t) = \frac{1 - M(0)}{1 - \dfrac{A(t)}{B^2(t)}}. \tag{9}$$

Thus, for the exponential initial spectrum $n_0(g) = a\exp(-gb)$, the behavior of the system is completely determined by solving two differential equations (8) with the initial conditions $A(0) = a$ and $B(0) = b$. Constraint (9) closes set (8).

The table presents the results calculated for $\chi = 1$, the initial spectral parameters $a = 0.5$ and $b = 1$, and coagulation with $Q = 2$. It is seen that calculations by the AerosGA code agree well with exact solution (8): the difference for $N(t)$ and $M(t)$ is no more than 6%.

The test of numerical methods of solving Eq. (1) for model (6) is a serious test of algorithms, because correct calculation of the complete evaporation of drops and high accuracy of calculation of spectral integrals are required. In particular, the direct application of the GA method for solving general equation (1) with rates $\nu(g)$ from Eq. (6) does not yield an acceptable result because of two circumstances. First, if $\varphi_0(g) = \text{const}$ enters into the set of basis functions, the boundary condition with the flux $n(0)\nu(0)$ is missing for the equation for $N(t) = L_0(t)$, and the use of step approximation (4) to this end is too rough. Second, if the basis functions begin with $\varphi_p(g)$, where $p > 0$, the complete evaporation and behavior of $N(t)$ are reproduced very inaccurately, because the set of equations for moments $L_m(t)$ is actually unclosed.

The set of the above methods and models realizes an integral approach to joint simulation of condensation and coagulation. This realization includes the GA method of solving coagulation equations on a variable grid, the particle method for calculating condensation kinetics, and the above algorithm of reproduction of nodes for transitions between calculations of coagulation and condensation. The efficiency of the AerosGA code based on this approach is illustrated both for a test that has an analytical solution in the form of strongly polydisperse spectra and for a new test with the sign-alternating condensation rate. The proposed realization of the integral approach is efficient and provides a prospect for developing fast methods of calculating the

Basic quantities for model (6) and coagulation with $Q = 2$

t	Calculation by Eq. (8)			AerosGA calculation		
	$g^*(t)$	$N(t)$	$M(t)$	$g^*(t)$	$N(t)$	$M(t)$
0	1	0.5	0.5	1	0.5	0.5
1	1.669	1.743–01	7.005–01	1.672	1.787–01	7.009–01
2	4.053	1.112–01	8.767–01	3.975	1.156–01	8.742–01
5	12.192	5.502–02	9.681–01	11.745	5.660–02	9.670–01
10	31.133	3.004–02	9.839–01	27.949	2.993–02	9.839–01
20	61.350	1.577–02	9.919–01	60.314	1.520–02	9.921–01
50	151.52	6.510–03	9.967–01	158.73	6.225–03	9.969–01

kinetics of the formation of particles in disperse systems.

ACKNOWLEDGMENTS

I am grateful to V.M. Povyshev for performing calculations. This work was supported by the International Science and Technology Center, project no. 1908.

REFERENCES

1. R. McGraw, Aerosol. Sci. Technol. **27**, 255 (1997).
2. V. N. Piskunov and A. I. Golubev, Dokl. Akad. Nauk **366**, 341 (1999) [Dokl. Phys. **44**, 323 (1999)].
3. V. N. Piskunov and A. I. Golubev, J. Aerosol Sci. **33**, 51 (2002).
4. G. I. Marchuk, *Methods of Splitting* (Nauka, Moscow, 1988).
5. V. N. Piskunov, *Theoretical Models of the Kinetics of Aerosol Formation* (RFYaTs-VNIIÉF, Sarov, 2000).
6. V. N. Piskunov, A. I. Golubev, J. C. Barrett, and N. A. Ismailova, J. Aerosol Sci. **33**, 65 (2002).
7. D. L. Wright, J. Aerosol. Sci. **31**, 1 (2000).
8. V. N. Piskunov and A. M. Petrov, J. Aerosol Sci. **33**, 647 (2002).
9. I. M. Lifshits and V. V. Slezov, Zh. Éksp. Teor. Fiz. **35**, 479 (1958) [Sov. Phys. JETP **8**, 331 (1959)].
10. V. N. Piskunov, Vopr. At. Nauki Tekh., Ser.: Teor. Prikl. Fizika, No. 1, 24 (1984).

Translated by R. Tyapaev

Doklady Physics, Vol. 49, No. 7, 2004, pp. 436–439. Translated from Doklady Akademii Nauk, Vol. 397, No. 3, 2004, pp. 337–341.

MECHANICS

Mechanism of the Crushing of Particles for Production of Submicron Powders of Refractory Compounds in a Pneumatic Circulation Apparatus

N. N. Belov, Yu. A. Biryukov, A. T. Roslyak, N. T. Yugov, and S. A. Afanas'eva

Presented by Academician V.N. Antsiferov February 18, 2004

Received February 27, 2004

The possibility of the wide variation of all basic parameters (density, strength, thermal conductivity, electrical resistance, viscosity, etc.) determining the functional and construction characteristics of ceramics is the fundamental advantage of these materials over metals. These materials are produced from fine-grained powders of refractory compounds (nitrides, carbides, oxides) that are calibrated in the particle sizes. The crushing and separation of such submicron powders in amounts ensuring their further profitable use for production of new construction and functional materials present a very urgent independent scientific and engineering problem. In this paper, we report some results of experimental and theoretical investigation of a new method for crushing refractory compounds that is based on high-speed flooded gas jets.

Current tendencies of the development of crushing equipment show that pneumatic methods, where a compressed gas with pressure 0.4–1.0 MPa is used, are most efficient for the production of submicron powders [1]. A new crushing method has been successfully realized in a pneumatic circulation apparatus by the action of incompletely widened flooded gas jets on a bulk layer of a material [2]. The work of circulation apparatuses with flooded jets is based on the controlled circulation motion of flows of the "gas + solid particles" system in closed volumes. The fundamental difference of this method from other available pneumatic crushing methods is the continuous withdrawal of the final material from the crushing region and the multiple circulation of the incompletely crushed material. In this method, particles of the material multiply interact with each other and are finally disintegrated.

Intense interaction between particles proceeds at the "jet–bulk layer" boundary due to large velocity gradient, because their relative velocities in this boundary region are equal to 100–300 m/s. At the same time, particles do not interact with the walls of the apparatus, which virtually excludes the crushing of impurities.

The controlled circulation motion of heterogeneous flows ensures simultaneous crushing and separation, which can be controlled independently from one another. The use of fitted separation elements of various types, together with the circulation of the two-phase medium in contours, allows the effective organization of the aerodynamics of a dust–gas flow in the separation region for the intensification of the countercurrent–centrifugal separation of particles and control of the separation boundary. In pneumatic circulation apparatuses, the opportune withdrawal of required-size particles and return of incompletely crushed particles to the working region increase the efficiency of the use of energy spent on crushing.

The crushing of refractory compounds was experimentally studied for aluminum oxide, carbide, silicon nitride, etc. Experimental industrial batches of submicron powders of all materials being tested were obtained, which corroborates the high efficiency of the pneumatic circulation crushing method. Processing of a large amount of experimental data and purposeful experiments reveal a number of features of the new method of crushing and separating particles.

The mass yield of target fractions was analyzed as a function of the rotor rotation speed for various working-gas rates (Fig. 1). It is found that, with an increase in the rotation speed up to about 4000 rpm, the mass yields of all target fractions decrease and then increase slightly. Moreover, the size and mass yield of target fractions are virtually independent of the working-gas rate. Therefore, gas dynamic structure changes at these regimes in the apparatus. Investigations of the degree of extraction of particles with sizes less than 5 μm show that this change promotes the formation of fine-grained fractions. To connect these facts with the gas dynamic structure produced by the rotor, the relative recirculation rate within the free volume of the apparatus was empirically estimated. It is found that, with an increase in the rotor rotation speed, the need for multiple recir-

Tomsk State University, Tomsk, 634050 Russia

1028-3358/04/4907-0436$26.00

culation decreases considerably and, correspondingly, the working-gas rate for extraction of the key fraction decreases.

Figure 2 shows the expenditures of the working gas (compressed air) on production of the required fractions in the pneumatic circulation apparatus and AFG mill manufactured by Hosokawa Micron Corporation [3]. As is seen in Fig. 2, energy expenditures in the pneumatic circulation apparatus are 30% lower for fractions of small sizes (e.g., 10 μm). These advantages of the new method of pneumatic processing of powders allow a decrease in energy expenditures and profitable technology for producing submicron powders.

Experimental investigations and their analysis made it possible to improve pneumatic circulation apparatuses and to ensure production of refractory-compound powders with a particle size of about 0.3 μm for construction and functional ceramics of aluminum oxide and zirconium oxide. The granulometric content was determined by electron and optic microscopes. Similar characteristics were also obtained by simultaneous crushing and separation of nitride, carbides and oxides of various elements, aluminum, nichrome, etc.

The pneumatic circulation method of crushing and separating initial components was applied to produce silicon powders with particle sizes of 1 μm and less. The resulting fractions are used to obtain silicon nitride and silicon carbide by high-temperature synthesis methods [3]. Analysis of the effect of the size of initial silicon particles shows that the process rate increases when the size decreases. A decrease in the particle size δ_{97} from 3 to 1 μm leads to an increase in the combustion rate by a factor of 1.5. Analysis of the product shows that the particle size does not increase. This result is important for technology of producing submicron powders of refractory silicon compounds, because the crushing of initial silicon is much easier than the crushing of its nitride.

The crushing mechanism is studied for aluminum oxide. The process of the destruction of particles is analyzed in two limiting cases in the framework of the mathematical model of the deformation and destruction of high-strength ceramic [4]. The first limiting case is the frontal impact of cylindrical particles whose linear size is much smaller than their diameters. In this case, the effect of lateral unloading waves on the deformation and destruction of particles can be disregarded, and the problem can be solved for a uniaxial strain state, which considerably simplifies analysis of shock phenomena. The second limiting case is the normal collision of spherical particles with a rigid wall, which corresponds to the collision of particles moving towards each other with half the velocity. In this case, the shape of particles strongly affects the process of crushing particles.

Figure 3 shows the results of numerical calculations for the collision between 100- and 250-μm particles with a velocity of 300 m/s. Figure 3a shows the distribution of the relative volume ξ of cavities over the target at the time when a spall is formed. Figure 3b shows the time dependence of stress σ_1 in the spall section. These figures enable one to determine the mechanism of the destruction of a material.

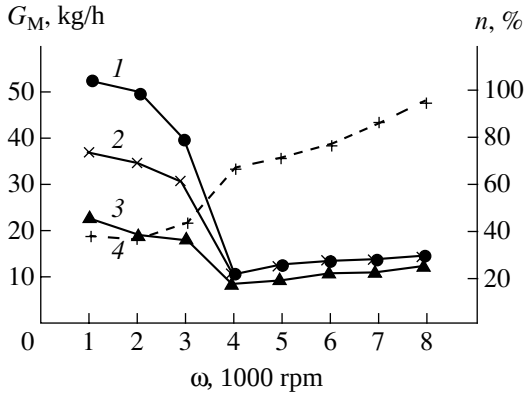

Fig. 1. Mass yield of target fractions vs. the rotor rotation speed for a working-gas rate of (*1*) 48, (*2*) 43, and (*3*) 38 m^3/h and (*4*) a particle-crushing degree of 5 μm.

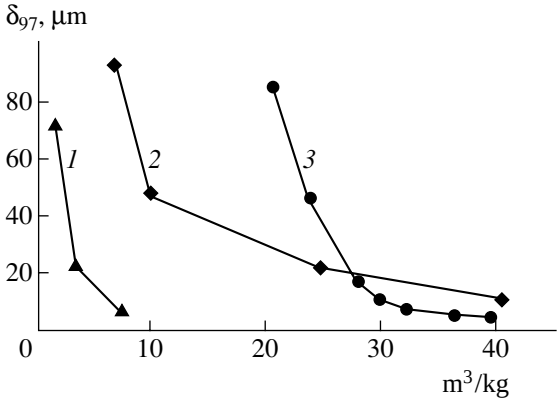

Fig. 2. Distribution of energy expenditures vs. the size of a required fraction for (*1*) alumina and (*2, 3*) corundum obtained with an (*1, 2*) AFG mill and (*3*) pneumatic circulation apparatus.

When microparticles collide with each other, shock waves propagate on both sides of the contact surface. Behind these shock waves, a steady flow is formed with stress $\sigma_1 = 4.4$ GPa and mass velocity $u = 150$ m/s. The intensity of shear stresses behind the shock fronts exceeds the threshold level. As a result, microcracks grow (shear destruction). At a time of 0.011 μs, the shock front in the incident particle reaches its free end surface and is reflected into the shock-compressed material in the form of an elastic unloading wave, reducing compression stress to zero. At 0.025 μs, the shock wave in the target particle also reaches the free surface. The unloading waves propagating from the free end surfaces of particles meet each other in the target particle at a distance of 120 μm from the contact surface at a time of 0.035 μs. The interaction between these waves causes tensile stresses ($\sigma_1 = -4.4$ GPa) and

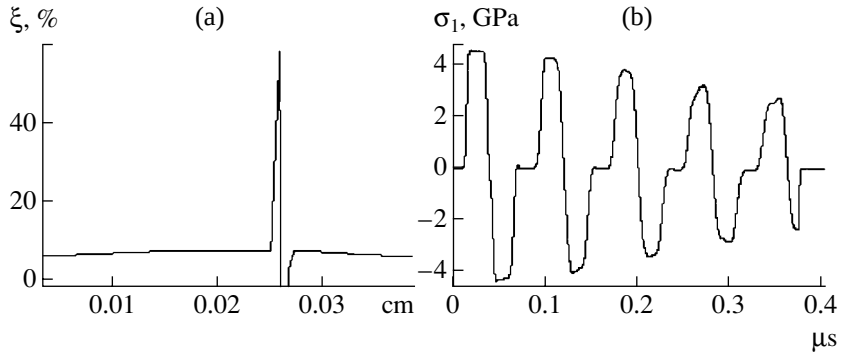

Fig. 3. (a) Distribution of the relative volume of cavities over a target at the time of the formation of a spall and (b) the time dependence of stress in the spall section.

the growth of microcracks, which are opened by tensile stresses. This opening leads to the relaxation of tensile stresses. At this stage of the impact interaction of microparticles, the spallation mechanism of destruction is realized.

The unloading wave propagating from the free end surface of the incident particle reaches the free end surface of the target particle at a time of 0.056 μs and is reflected into the material in the form of an elastic compression wave. Behind its front, tensile stresses increase to zero and microcracks cease to grow. The unloading wave propagating from the free end surface of the target particle reaches the free end surface of the incident particle at a time of 0.075 μs. The two oppositely propagating shock waves formed when the unloading waves are reflected from the free end surface meet each other at a time of 0.08 μm near the contact surface. Behind their fronts, steady flows are formed with stress $\sigma_1 = 4.2$ GPa and mass velocity $u = 145$ m/s. In these flows, the growth of microcracks through the shear mechanism (spallation destruction) is renewed. At further stages of the impact interaction between microparticles, the shock waves reach the free end surfaces of incident and target particles and are reflected from them, forming the unloading waves whose interaction causes tensile stresses and the growth of microcracks. The target particle is destroyed at 0.38 μs at a distance of about 160 μm from the contact surface. The target particle splits into two particles damaged with microcracks. The thickness of the separated particle is equal to 100 μm.

The above shock-wave mechanism of the destruction of microparticles is well manifested in the diagram of stresses σ_1 for a plate at a distance of 160 μm from the contact surface. This diagram provides information on the material loading development in the destruction region. The material in this section undergoes five loading cycles before the length of microcracks reaches the critical value and destruction occurs.

Material regions damaged with cracks are easily identified by the distribution of the relative volume of cavities in the incident and target particles. The sizes of cracks are close to the critical value near the spall surface. The secondary collision of the incident and target particles formed in the impact process with other particles leads to the crushing of the former particles for rather low impact velocities.

To reveal the scale effect of the above shock-wave crushing mechanism, the collision of spherical particles with a rigid wall is simulated for particle diameters 0.1, 1, and 10 mm and velocities 100 and 300 m/s. The wave pattern observed in the collision of a spherical particle with the rigid wall differs significantly from the wave pattern under a one-dimensional frontal impact. At the initial time, the ball touches the wall only at one point. Upon deforming a spherical element, the area of the contact surface increases, the shock wave is formed in the ball, and a complex stress–strain state arises.

Analysis of the results shows that a 0.1-mm-diameter particle is not destroyed for these collision velocities. A 1-mm-diameter particle is partially destroyed for a velocity of 300 m/s. A 10-mm-diameter particle is destroyed partially and completely for velocities 100 and 300 m/s, respectively. Figure 4 shows the development of the destruction of a 10-mm-diameter particle for a collision velocity of 300 m/s in the form of isometric projections of a half of the particle.

Multiple collisions (up to quadruple) of undestroyed or partially damaged particles are also simulated. Only one-half of the volume of a particle that has a diameter of 0.1 mm and a velocity of 300 m/s is destroyed in quadruple collisions with the rigid wall. A particle that has a diameter of 1 mm and the same velocity is almost completely destroyed already in a repeated collision.

Thus, the destruction of a smaller particle requires a higher collision velocity, because the compression wave formed in the larger particle, as well as the unloading waves that are generated by this wave and lead to the fragmentation of the particle, has higher intensity. Moreover, the loading time increases strongly upon an increase in the particle size. As a result, the growth of microcracks lasts longer, and microcracks grow up to the critical value.

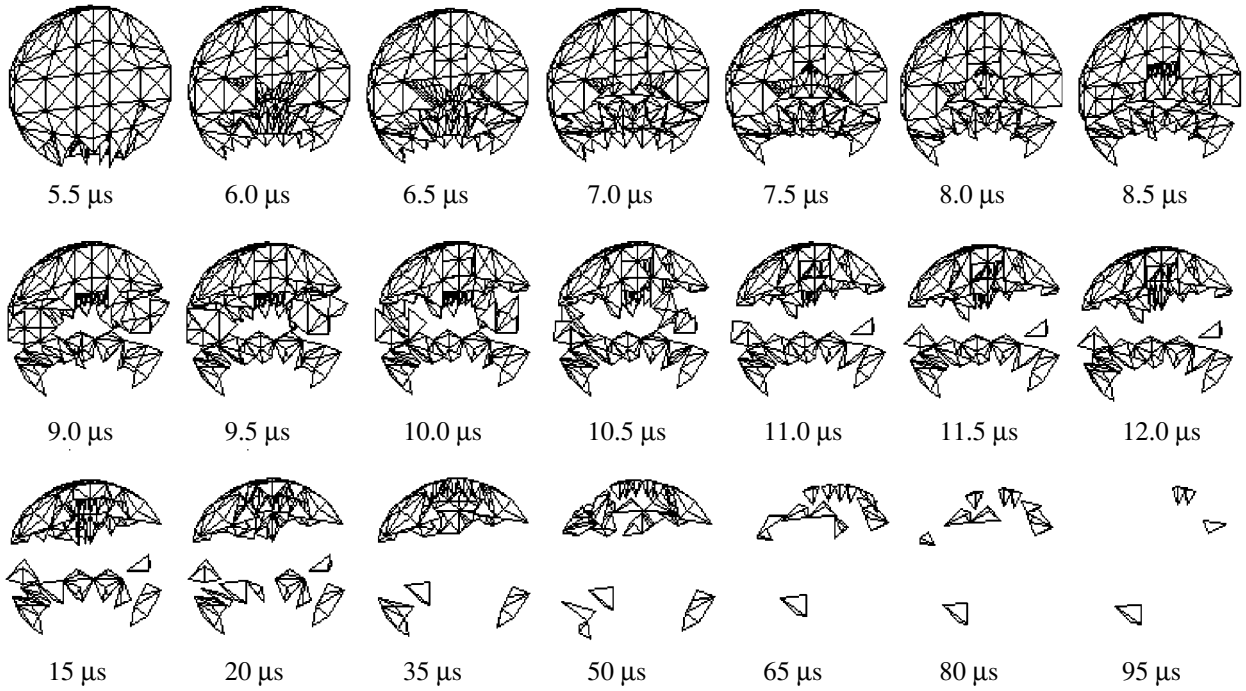

Fig. 4. Development of the destruction of a particle.

The results show that the pneumatic circulation method in combination with other processes can provide the basis for developing high-efficiency technologies for producing new ceramic materials for numerous applications. The mathematical model ensures the possibility of analyzing in detail mechanisms of the destruction of microparticles in the process of their multiple interactions.

ACKNOWLEDGMENTS

This work was supported by the Russian Foundation for Basic Research (project nos. 01-01-00821 and 01-01-00813).

REFERENCES

1. P. M. Silverberg, S. Sharon, and M. Homing, Chem. Eng. **105** (123) (1998).
2. Yu. A. Biryukov, A. T. Roslyak, P. N. Zyatikov, *et al.*, Patent No. 1273193, Byull. Izobret., No. 18 (1997); Inventor's Certificate, Byull. Izobret., No. 44 (1996).
3. Yu. Biryukov, A. Roslyak, L. Bogdanov, and M. Ziatdinov, in *Proceedings of the 32nd International ICT-Conference on Energetic Materials: Ignition, Combustion, and Detonation, Karlsruhe, 2001*.
4. S. A. Afanas'eva, N. N. Belov, V. F. Tolkachev, *et al.*, Dokl. Akad. Nauk **368**, 477 (1999) [Dokl. Phys. **44**, 683 (1999)].

Translated by R. Tyapaev